Refining simulated mineral dust composition through modified size distributions: dual validation with mineral-specific and elemental observations

Sofía Gómez Maqueo Anaya[1], Sudharaj Aryasree[2], Konrad Kandler[2], Eduardo José dos Santos Souza[1], Khanneh Wadinga Fomba[1], Dietrich Althausen[1], Maria Kezoudi[3], Matthias Faust[1], Bernd Heinold[1], Ina Tegen[1], Moritz Haarig[1], Holger Baars[1], and Kerstin Schepanski[1,4]

[1]Leibniz Institute for Tropospheric Research (TROPOS), Leipzig, Germany
[2]Institute of Applied Geosciences, Technical University of Darmstadt, Germany
[3]Climate and Atmosphere Research Centre (CARE-C), The Cyprus Institute, Nicosia, Cyprus
[4]Free University of Berlin, Berlin, Germany

Correspondence: Sofía Gómez Maqueo Anaya (maqueo@tropos.de)

Abstract. Two 2022 measurement campaigns in Cape Verde provided a unique opportunity to collect mineral dust aerosols from multiple Saharan source regions and characterize their composition. Mineral dust aerosols comprise a complex assemblage of minerals with distinct physico-chemical properties, leading to differentiated climatic impacts through interactions with radiation, cloud microphysics, and atmospheric chemistry. A crucial physical property governing these interactions is the particle size distribution (PSD), which strongly influences aerosol optical properties, transport, and deposition. Although contemporary atmospheric models have begun integrating mineralogical data into their dust aerosol representations, implementation faces complications due to variations in dust emission parameterizations, making some models more compatible with existing soil mineralogical databases than others.

This work addresses the challenges encountered when incorporating mineralogical information into the COSMO5.05-MUSCAT atmospheric model, which employs a dust emission scheme based on Marticorena and Bergametti (1995). We present an improved approach that refines the translation of mineralogical soil PSDs into emitted aerosol PSDs. The revised implementation is evaluated using historical Saharan dust measurements and new mineralogical observations from the JATAC2022 and DUSTRISK2022 campaigns. Model performance is assessed using a dual validation framework considering both mineral-resolved and elemental composition. The elemental validation approach provides complementary constraints that expose discrepancies in internal mixing assumptions and reveal limitations invisible to mineral-only comparisons. Results indicate that the proposed modification substantially improves representation of phyllosilicates (illite, kaolinite, and smectite), quartz, and feldspar, while biases in iron, calcium, and magnesium highlight fundamental challenges in representing the heterogeneous internal structure of natural dust particles.

1 Introduction

Mineral dust aerosol is the most abundant atmospheric aerosol type by mass (Kinne et al., 2006) and exerts widespread influence on the Earth system. By scattering and absorbing solar and terrestrial radiation, dust modifies atmospheric heating rates, alters cloud microphysical processes, and perturbs the surface energy balance (Stocker et al., 2013; Kok et al., 2023). Despite this recognized role, large uncertainties remain in quantifying the net radiative forcing by dust. These uncertainties arise from the complex variability of dust properties during emission and transport, including particle size distribution (PSD), morphology, mixing state, and mineralogical composition (Huneeus et al., 2011; Mahowald et al., 2014; Di Biagio et al., 2020).

Mineralogical composition has emerged as a key factor in constraining dust–climate interactions. Different minerals govern how dust interacts with radiation, clouds, and other atmospheric constituents. For instance, small variations in the abundance of iron oxide-bearing minerals can strongly amplify shortwave absorption and alter dust's radiative properties (Balkanski et al., 2007; Gómez Maqueo Anaya et al., 2025; Li et al., 2024; Miffre et al., 2023; Obiso et al., 2024; Sokolik and Toon, 1999; Zhang et al., 2024), while silicate minerals differ in their potential to act as ice-nucleating particles (INPs) or cloud condensation nuclei (CCN) under varying conditions (Chatziparaschos et al., 2023; Harrison et al., 2019; Kelly et al., 2007; Murray et al., 2012). Yet, most chemistry transport models treat dust as homogeneous with respect to its composition, neglecting the strong spatial and temporal variability of mineral fractions. This simplification introduces biases in estimates of dust absorption, cloud interactions, and downstream impacts such as nutrient deposition (Kok et al., 2023).

Incorporating mineralogical detail into models is therefore essential, but it depends critically on how the PSD of individual minerals in soils is represented. The PSD controls not only transport and deposition but also the mineral dust particles' interaction with radiation. A central challenge is that the PSD of airborne dust does not directly reflect the PSD of the parent soil: during emission, processes such as soil texture effects, interparticle cohesion, wind friction velocity, and fragmentation and saltation dynamics reshape the particle size distribution (Marticorena and Bergametti, 1995; Kok, 2011). These nonlinear processes lead to size-dependent shifts in mineralogical composition, making the link between soil and atmospheric mineralogy far from trivial.

The particle size distribution of mineral dust fundamentally governs its atmospheric residence time and transport dynamics. Coarse-grained minerals such as quartz, feldspars, and calcite tend to be removed quickly by gravitational settling, resulting in higher concentrations near source regions. In contrast, finer clay-sized phyllosilicates, defined herein as the group of illite, kaolinite, and smectite, remain suspended for longer periods and thus constitute a major fraction of the dust transported to remote areas (Lawrence and Neff, 2009).

Despite the importance of these size-dependent dynamics, the Soil Mineral Atlases (SMAs), a generic term for databases describing the mineralogical composition of soils that are currently employed in atmospheric models, rely on a simplified classification of soil mineralogy into only two size fractions, clay (defined as particles with diameters up to 2.5 μm) and silt (particles with diameters between 2.5 to 50 μm) (diameter size ranges follow the convention used by Nickovic et al. (2012)). This framework introduces structural uncertainties and subsequent biases in model simulations. A notable consequence of this resolution limit is the representation of quartz; by assuming a constant mineral proportion across broad size ranges, models fail to capture the size-dependent distributions observed in empirical studies (Kandler et al., 2007, 2009; Panta et al., 2023). This

often results in a systematic overestimation of quartz mass fractions in coarser bins and a corresponding underestimation in finer fractions (Perlwitz et al., 2015a, b).

To mitigate these discrepancies, several models have moved toward mineral-specific PSD transformations based on the Brittle Fragmentation Theory (BFT) (Kok, 2011). This approach provides a semi-direct framework for predicting size-resolved emission fluxes (e.g., Gonçalves Ageitos et al., 2023; Scanza et al., 2015; Perlwitz et al., 2015a). However, a significant number of models continue to rely on the parameterization scheme developed by Marticorena and Bergametti (1995). While robust for bulk soil properties, this scheme cannot directly provide mineral-specific fluxes, particularly when constrained by the incomplete mineralogical information inherent in standard SMAs. Assessing the implications of these contrasting emission strategies is essential for accurate mineral-resolved simulations, yet systematic evaluations of their impact remain limited.

In a previous study, Gómez Maqueo Anaya et al. (2024) implemented a mineralogical composition module for Saharan dust simulations within COSMO5.05–MUSCAT (COnsortium for Small-scale MOdelling v5.05 - MUltiScale Chemistry Aerosol Transport). Building on that work, this article addresses a central methodological question: how should the transformation of the PSD from soil to atmosphere be represented within the COSMO5.05–MUSCAT dust emission framework to ensure a realistic reproduction of mineralogy-based dust properties? To this end, we evaluate two PSD transformation approaches based on the Marticorena and Bergametti (1995) emission scheme, coupled with the mineralogical database GMINER (Nickovic et al., 2012).

Specifically, we contrast two modeling schemes, hereafter referred to as the 'original' and 'modified' approaches. The 'original' scheme, following Gómez Maqueo Anaya et al. (2024), maps the mineral soil PSD directly onto the aerosol size distribution. While this method adequately represents clay-sized minerals, it shows marked discrepancies for silt-sized fractions when compared with observations. To improve this representation, the 'modified' scheme introduces refinements to the treatment of mineral soil PSD via a redistribution of mineral fractions informed by the application of the BFT. The details of this modification, along with the specific model configurations and experimental runs, are described in Section 2.

The performance of the two schemes is assessed against a multi-level observational dataset. We first utilized a compilation of regional North African mineralogical measurements of in-situ aerosol samples to evaluate broad mineralogical patterns and enable a direct comparison between the implemented schemes. This is followed by a high-resolution comparison with concurrent in-situ observations from two campaigns in Cabo Verde: the Joint Aeolus Tropical Atlantic Campaign (JATAC, June 2022) and DUSTRISK (January–February 2022). JATAC 2022 provides size-resolved measurements of both mineralogical composition and elemental mass concentrations. Similarly, DUSTRISK 2022 offers size-resolved elemental mass concentrations, allowing for a consistent evaluation of the model's chemical tracers. The specific measurement methodologies, instrumentation for size-segregation, and associated uncertainties for these campaigns are detailed in Section 3.

The strategy for model evaluation, including the metrics used for validation and the procedure for comparing grid-cell results to point measurements, is outlined in Section 4. Following this, the validation results are presented through a tiered approach categorized by analytical scale. Section 5.1 focuses on mineralogical comparisons, beginning with the regional North African compilation and followed by a detailed assessment of the JATAC 2022 results. Section 5.2 then provides a focused analysis of elemental composition, evaluating the model against the 2022 campaigns, JATAC and DUSTRISK 2022. This tiered approach

allows us to assess whether the BFT-informed redistribution effectively bridges the gap between soil mineralogy and airborne dust composition across different transport conditions and measurement methodologies.

2 Model description and parametrizations

2.1 COSMO5.05-MUSCAT

The chemistry transport model used in this study is the MUltiScale Chemistry Aerosol Transport (MUSCAT) coupled online with the COnsortium for Small-scale MOdelling (COSMO) v5.05 model. COSMO, developed by the German Weather Service (Deutscher Wetterdienst, DWD), is a non-hydrostatic regional weather prediction model that solves the fundamental equations of atmospheric dynamics on a terrain-following grid (Baldauf et al., 2011). MUSCAT is the online-coupled chemistry transport component, computing the atmospheric transport of aerosols through time-dependent mass balance equations driven by COSMO meteorological fields (Heinold et al., 2011; Wolke et al., 2012). In this work, mineral dust aerosols are represented as passive tracers, i.e., they are not subject to chemical aging or chemically reactive transformations.

The coupled atmosphere-aerosol model system, COSMO-MUSCAT, has been widely applied and evaluated for Saharan dust studies. Previous validation efforts have demonstrated its capability to reproduce dust source activation, transatlantic transport, and regional dust transport under different meteorological conditions (Heinold et al., 2011; Schepanski et al., 2009; Tegen et al., 2013; Schepanski et al., 2016, 2017). The specific configuration used here has been further evaluated against atmospheric dust loading observations in Gómez Maqueo Anaya et al. (2024) and Gómez Maqueo Anaya et al. (2025).

The atmospheric life cycle of dust aerosols in MUSCAT is represented through a set of physical parameterizations dynamically coupled to COSMO meteorology and updated at every advection step. The main processes include: (1) dust emission, parameterized following Tegen et al. (2002) with modifications to incorporate mineralogical soil fractions as described in Gómez Maqueo Anaya et al. (2024); (2) aerosol transport, solved using a third-order upwind advection scheme with time-splitting integration (Wolke and Knoth, 2000); and (3) aerosol deposition, accounting for both dry and wet removal processes. Dry deposition is parameterized following the formulations of Seinfeld and Pandis (2016) and Zhang et al. (2001), while wet deposition (including in-cloud scavenging or rainout, and below-cloud scavenging or washout) follows the approaches of Berge (1997) and Jakobsen et al. (1997), with detailed implementation described in Heinold et al. (2011).

2.2 Dust emission scheme

Dust emission is a non-linear process initiated when near-surface wind velocity generate sufficient vertical shear stress at the soil surface to initiate particle mobilization. In COSMO-MUSCAT, threshold friction velocities are calculated following the parameterization of Marticorena and Bergametti (1995), which accounts for size-resolved soil particle mobilization and depends on soil texture, surface roughness, vegetation, and soil moisture.

Emission fluxes are then computed interactively using the scheme of Tegen et al. (2002), first implemented in COSMO-MUSCAT by Heinold et al. (2007). Fluxes scale with the cube of the wind friction velocity, derived from COSMO-simulated

near-surface winds, and are further modulated by vegetation cover and soil moisture. Particle uplift occurs when the effective friction velocity exceeds the size-dependent threshold (U_{t}^*), which is controlled by the erodible particle diameter (D_{p}), the aerodynamic roughness length of the total surface (Z_0), and the smoother, erodible fraction roughness length ($z_{0\mathrm{s}}$).

To account for the sheltering effect of roughness elements, a drag partitioning approach is utilized. This method defines an effective friction velocity (U_{t}^*), representing the total friction velocity required to mobilize size-dependent particles on a rough surface. It is related to the smooth-surface threshold friction velocity (U_{ts}^*), which is the threshold required for mobilizing the same particles under idealized, flat, conditions, via:

$$U_{\mathrm{t}}^*(D_{\mathrm{p}}, Z_0, z_{0\mathrm{s}}) = \frac{U_{\mathrm{ts}}^*(D_{\mathrm{p}})}{f_{\mathrm{eff}}(Z_0, z_{0\mathrm{s}})}, \tag{1}$$

where f_{eff} is the effective drag partition factor (ranging from 0 to 1). This factor accounts for the reduction in wind erosive potential due to surface roughness and it is calculated following Marticorena and Bergametti (1995) as:

$$f_{\mathrm{eff}}(Z_0, z_{0\mathrm{s}}) = 1 - \left[\ln\left(\frac{Z_0}{z_{0\mathrm{s}}}\right) / \ln\left(0.35\left(\frac{10}{z_{0\mathrm{s}}}\right)^{0.8}\right)\right]. \tag{2}$$

For bare desert surfaces, the aerodynamic roughness length (Z_0) is prescribed as 0.001 cm, following the recommendation of Darmenova et al. (2009), while $z_{0\mathrm{s}}$ is obtained from global satellite-derived dataset (Prigent et al., 2005). The value of U_{ts}^* is calculated as a function of particle diameter (D_{p}), particle density, and air density (ρ_{a}), representing a balance between aerodynamic and gravitational forces.

The actual surface friction velocity exerted by the atmosphere (U^*) is estimated from COSMO's 10-meter wind speed components (u_{10}, v_{10}) and air density. These are combined to determine an effective wind speed at height Z, denoted as $U(Z)$. Assuming adiabatic conditions and a logarithmic wind profile within the boundary layer, U^* is calculated as:

$$U^* = \frac{U(Z)\kappa}{\ln\left(\frac{Z}{Z_0}\right)} \tag{3}$$

where $\kappa = 0.4$ is the Von Karman's constant, and Z represents the height of the first model layer.

Dust emission is triggered when this surface friction velocity exceeds the size-dependent threshold friction velocity ($U^* \geq U_{\mathrm{t}}^*$). This process is further modulated by local soil conditions such as moisture, which is accounted by an additional coefficient in the threshold calculation, following Fécan et al. (1999).

Once the threshold is surpassed, the emitted flux is represented as the horizontal particle flux (G), which scales with the cube of the friction velocity and accounts for the soil particle size distribution:

$$G = \frac{\rho_{\mathrm{a}}}{\mathrm{g}} \cdot U^{*3} \cdot \sum_i \left[\left(1 + \frac{U_{\mathrm{t}}^*(D_{\mathrm{pi}}, Z_0, z_{0\mathrm{s}})}{U^*}\right)\left(1 - \frac{U_{\mathrm{t}}^{*2}(D_{\mathrm{pi}}, Z_0, z_{0\mathrm{s}})}{U^{*2}}\right) \cdot B_{\text{rel-i}}\right] \text{for } U^* \geq U_{\mathrm{t}}^*, \tag{4}$$

where g is gravitational acceleration, and $B_{\text{rel-i}}$ represents the relative basal surface area of size fraction i. In MUSCAT, the soil is represented by 196 discrete size fractions.

Because the threshold friction velocity does not scale linearly with particle diameter, an accurate representation of the soil size distribution is required. In the Marticorena and Bergametti (1995) parametrization, the soil particle mass size distribution

Table 1. Definition of MUSCAT five independent size classes for mineral dust aerosol transport. Their size limits are indicated.

Bin name	Diameter range
BIN 01	0.2 - 1 μm
BIN 03	1 - 3 μm
BIN 09	3 - 9 μm
BIN 26	9 - 26 μm
BIN 80	26 - 80 μm

(PSD) is modeled using a multi-modal log-normal distribution:

$$\frac{\mathrm{d}m(D_\mathrm{p})}{\mathrm{d}\,\ln(D_\mathrm{p})} = \sum_{j=1}^{n} \frac{m_j}{\sqrt{2\pi}\ln(\sigma_j)} \exp\left(\frac{(\ln D_\mathrm{p} - \ln MMD_j)^2}{-2\ln^2\sigma}\right). \tag{5}$$

where j denotes the size mode (clay, silt, sand in the present MUSCAT setup) m_j is the mass fraction of mode j, σ is the geometric standard deviation (set to 2.0 independent of the mode), and MMD_j are the mass median diameters, set to 2.0 μm (clay), 15.0 μm (silt), and 150.0 μm (sand), respectively.

To determine the basal (projected) surface area distribution, the PSD is transformed assuming spherical particles of uniform density:

$$\mathrm{d}B_\mathrm{t}(D_\mathrm{pi}) = \frac{\mathrm{d}m(D_\mathrm{pi})}{\frac{2}{3}\rho D_\mathrm{pi}}. \tag{6}$$

The total basal surface area (B_t) is obtained by integrating Eq. (6) across all particle sizes. Normalizing $\mathrm{d}B_\mathrm{t}(D_\mathrm{pi})$ by B_t yields the relative basal surface area distribution $B_\mathrm{rel\text{-}i}$, which is used in Eq. (4) to allocate the horizontal flux across particle sizes.

Saltation and particle bombardment processes (Marticorena and Bergametti, 1995) are incorporated by iteratively adjusting $B_\mathrm{rel\text{-}i}$ for each size class, accounting for the momentum transfer from saltating particles to finer dust grains. Following this adjustment, the total horizontal flux is computed.

The fraction of the horizontal flux that becomes airborne is parameterized as a vertical dust flux (F):

$$F = \omega \cdot A_\mathrm{eff} \cdot G \cdot (1 - A_\mathrm{snow}) \cdot I_\theta, \tag{7}$$

where ω is the sandblasting efficiency, prescribed per soil type based on the local clay, silt, and sand fractions (Tegen et al., 2002). A_eff denotes the erodible surface area, A_snow is the snow-covered fraction, and I_θ represents a soil moisture correction following Fécan et al. (1999). The vertical flux is then partitioned into five transport-relevant size bins (Table 1) to generate size-resolved dust fluxes for atmospheric injection.

The overall magnitude and spatial variability of emissions are determined by the interplay of these surface conditions. The influence of vegetation cover on A_eff is threshold-dependent. In desert regions, dust emission is inhibited once fractional vegetation cover exceeds 0.5; below this threshold, the erodible area is scaled linearly to account for the partial sheltering of the

surface (Tegen et al., 2002). Similarly, I_θ reduces emissions linearly once soil moisture exceeds a critical threshold determined. While snow cover also inhibits dust emissions, its parametrization is deactivated in this model configuration given its negligible influence over the Sahara Desert. Together with the particle size distribution and surface roughness, these factors control the efficiency and spatial heterogeneity of dust emissions in the model.

2.3 Mineralogical composition modification

In the 'original' approach by Gómez Maqueo Anaya et al. (2024), mineralogical fractions are prescribed by directly mapping the mineral soil particle size distribution (PSD) from GMINER (Nickovic et al., 2012) onto the mineral-resolved aerosol PSD as represented by the upper panel of Fig. 1. A key limitation of this approach is that the modifications to the bulk PSD caused by the emission process do not affect the mineral-resolved PSD. This overlooks the fact that the emission process explicitly alters the overall dust PSD, as predicted by dust emission theories (Kok et al., 2012; Marticorena and Bergametti, 1995; Shao et al., 2011).

This inconsistency stems from the structure of GMINER in combination with Marticorena and Bergametti (1995)'s emission scheme, since GMINER provides mineralogical mass fractions only for the finest soil classes (silt and clay). These are assumed to represent the airborne dust range, given their capacity to remain suspended for several days. However, the emission scheme of Marticorena and Bergametti (1995) (Eqs. (5)–(6)) requires the full soil PSD to represent saltation and bombardment processes. Larger soil particles, although not staying airborne, are essential because their impacts release smaller fragments that otherwise could not overcome interparticle cohesion forces via wind induced friction velocity only (Marticorena and Bergametti, 1995; Iversen and White, 1982).

Consequently, a consistent application of the Marticorena and Bergametti (1995) scheme is not possible with GMINER alone, since the database lacks information on the coarser soil fractions. Figure 2 illustrates this limitation for a representative Saharan grid cell, highlighting the substantial portion of the soil PSD that is missing when mineral fractions are restricted to only the two finest classes.

The emission scheme inherently favors silt-sized particles, which require relatively low wind stress for entrainment and are small enough to remain airborne, as illustrated by the threshold friction velocity function (in Fig. 1 of Marticorena and Bergametti (1995)). This aerodynamic preference becomes problematic when GMINER assigns minerals exclusively to silt or clay size classes. Treating these mineral-resolved PSDs as representative of the full soil PSD within the Marticorena and Bergametti (1995) framework introduces systematic biases: clay-sized minerals experience artificially suppressed emissions due to high cohesion thresholds that rely on larger saltating particles to be broken, while silt-sized minerals are prone to overestimation in the absence of coarser, non-erodible grains. Accurate dust emission calculations therefore require a complete soil PSD, where larger particles mobilize finer fractions via saltation bombardment (Kok et al., 2012; Marticorena and Bergametti, 1995). This issue is compounded by the methodology used to construct GMINER: wet sieving mechanically disaggregates soil samples, increasing the apparent fraction of clay-sized particles relative to undisturbed soils (Perlwitz et al., 2015a). While airborne clay-sized fractions generally match source soils and are preserved during transport (Caquineau et al., 1998; Lafon et al., 2004), silt-sized mineral distributions show poorer agreement, partly due to biases introduced by wet-sieving (Perlwitz et al., 2015a).

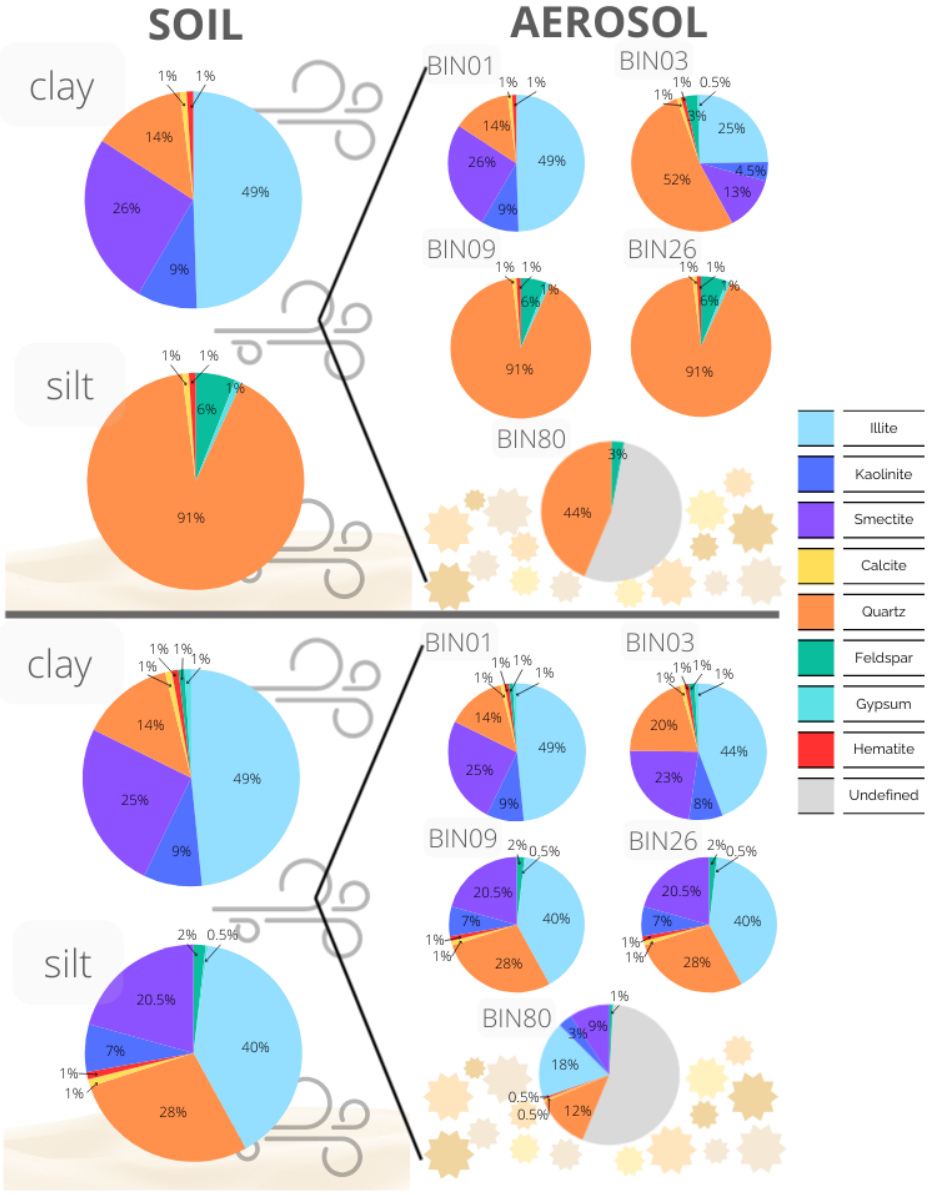

Figure 1. Mineralogical composition of soil and emitted dust particles. Larger pie charts represent the mineral fractions in the soil distribution, where clay is defined as particles with diameters below 2.5 µm and silt particles between 2.5 µm and 50 µm. Smaller pie charts represent the mineral fractions of aerosols per size bin as classified in MUSCAT (Table 1). Particles exceeding 50 µm diameter are not classified by mineral component and are labeled as "undefined". The upper panel shows the 'original' mineral soil PSD as obtained by GMINER and the subsequent mineral fractions in the aerosol bins mimicking that distribution. The lower panel shows the modifications to the soil mineralogy distribution and resulting aerosol fractions following the parametrizations of Perlwitz et al. (2015a) and Gonçalves Ageitos et al. (2023).

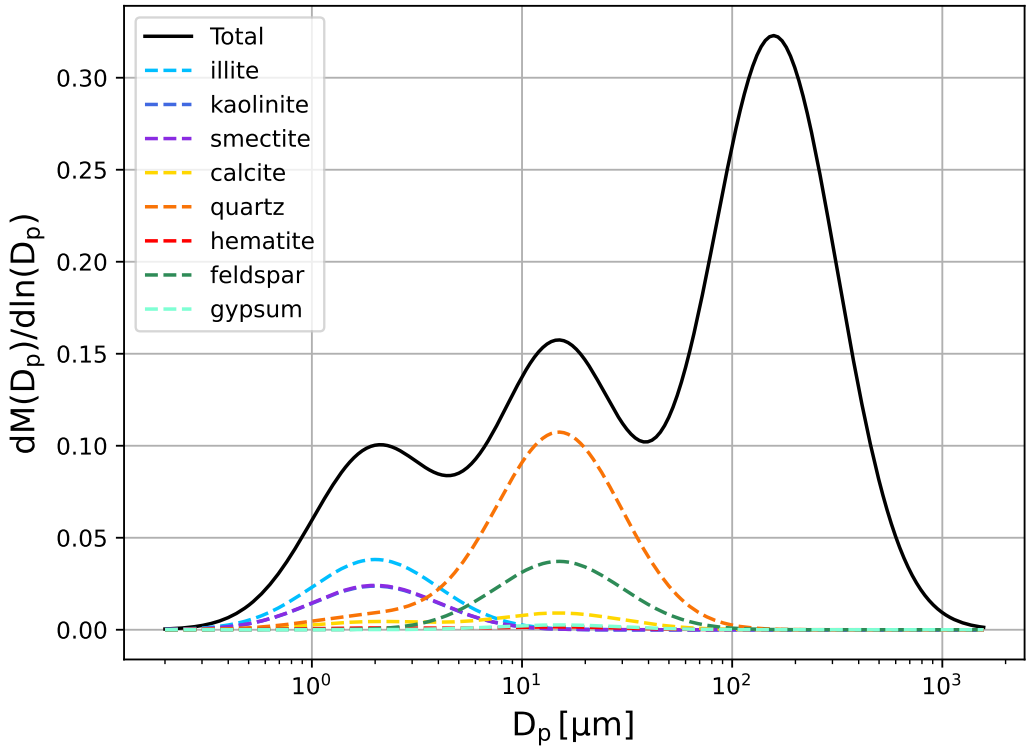

Figure 2. Mass size distribution of soil particles at a representative Saharan grid cell (22.45°N, 20.9°E). The black solid line represents the total distribution obtained from the SoilGrids database (Poggio et al., 2021), exhibiting three distinct modes corresponding to clay, silt and sand fractions. Dashed colored lines indicate the mineral specific mass size distributions as described by the GMINER database. Figure from Gómez Maqueo Anaya (2025)

.

To address these issues, several modeling studies have incorporated mineral-specific transformations from soil to aerosol PSDs (e.g., Perlwitz et al., 2015a, b; Gonçalves Ageitos et al., 2023; Pérez García-Pando et al., 2016; Scanza et al., 2015; Li et al., 2021). These approaches build on the Brittle Fragmentation Theory (BFT) of Kok (2011), which posits that for the finest particles, the emitted size distribution is largely independent of soil properties and wind speed. BFT conceptualizes emission as a sequence of energetic collisions between saltating aggregates, producing fragments that predominantly fall below a characteristic size threshold. The resulting particle number concentration N is inversely proportional to the square of the particle diameter D_p, modulated by an exponential cutoff, as expressed in the following relation:

$$\frac{dN}{dlnD_\mathrm{p}} \propto \frac{1}{D_\mathrm{p}^2} exp\left[-\left(\frac{D_\mathrm{p}}{D_\mathrm{c}}\right)^3\right] \mathrm{for} D_\mathrm{p} > D_\mathrm{s}, \tag{8}$$

where D_s represents a scalar diameter within the "indivisible" size range. Particles at or below this scale are considered primary grains resistant to further fragmentation due to inherent particle cohesion. Following Kok (2011), the probability of finding such indivisible grains at a specific size D_s is dictated by the PSD of the fully dispersed, wet-sieved soil. Incorporating this distribution, the emitted number size distribution is formalized as:

$$\frac{dN}{dlnD_p} = \frac{1}{c_N D_p^2} exp\left[-\left(\frac{D_p}{D_c}\right)^3\right] \int_0^{D_p} p(D_s) dD_s, \tag{9}$$

where c_N is a normalization factor, and $p(D_s)$ represents the probability density function derived from the wet-sieved PSD. In this integral, D_s serves as the scalar integration variable representing the diameters of the constituent primary grains. This formulation captures the physical constraint that an emitted aggregate of size D_p can only be composed of indivisible components smaller than or equal to itself $D_s \leq D_p$. The integral term (the cumulative distribution function of the soil minerals) thus reduces the emission of small particles if the soil lacks sufficient fine indivisible grains, while the exponential cutoff suppresses the emissions of very large diameters.

The BFT posits that the emitted number concentration of small dust particles is largely independent of the undispersed soil size distribution, with the characteristic aggregate diameter (D_c) estimated at 12 ± 1 μm (Kok, 2011). In this framework, the PSD of emitted aggregates is skewed toward larger diameters compared to wet-sieved soil, consistent with observations by Kandler et al. (2009) and Enete (2012), which indicate that saltation-driven fragmentation preserves a greater fraction of mass in the silt-size range than suggested by wet-sieved samples. Perlwitz et al. (2015a) further show that roughly 45% of the silt-sized emitted mass originates from aggregated indivisible particles that would be classified as clay-sized in wet-sieved soils. To reconcile this discrepancy, they proposed an empirical correction that reallocates a fraction of clay-sized minerals from wet-sieved soils to the silt fraction, particularly phyllosilicates (illite, kaolinite, and smectite), which are categorized in GMINER exclusively in clay size classes but contribute to silt-sized emissions in reality.

This adjustment is quantified using Equation (9) to derive a generalized ratio of emitted clay- to silt-sized particles, assumed to be spatially invariant and independent of local soil conditions. This simplifying assumption has been adopted in several modeling studies (Albani et al., 2014; Perlwitz et al., 2015a, b; Scanza et al., 2015; Pérez García-Pando et al., 2016; Gonçalves Ageitos et al., 2023). However, it applies only to particles below 20 μm, as larger particles are more sensitive to site-specific emission factors such as wind speed, soil properties, and surface roughness. Since GMINER defines the silt class up to 50 μm, a further adjustment is needed for particles in the 20–50 μm range. Perlwitz et al. (2015a) addressed this by scaling the clay contribution using measurements from Kandler et al. (2009), which provided empirical data on the coarse-mode mineral distribution of freshly emitted dust. Using Equation (9), they estimated a clay-to-silt ratio of 0.05 for diameters below 20 μm. When integrated over the full 0-50 μm range and volume-normalized to account for the coarser fraction, this corresponds to approximately 1.3% of the total emitted mass being attributed to the clay mineral fraction.

This methodology rests on two critical assumptions. First, it assumes that the PSD measured at Tinfou by Kandler et al. (2009) is representative of other dust source regions. While this may not hold universally, the observed increase in silt fraction with particle diameter is consistent with the physical principle that the threshold friction velocity for emission decreases with

particle size (Marticorena and Bergametti, 1995; Iversen and White, 1982). The approach also assumes that the emitted PSD is primarily determined by mineral-specific fragmentation, neglecting wind speed variations. This assumption is reasonable for particles below 20 μm, where Eq. (9) offers a reliable approximation, but becomes less reliable for coarser particles where emission dynamics are more sensitive to environmental conditions. Second, the model neglects modifications to the PSD caused by gravitational settling during transport to the Tinfou observation site. This simplification is justified by focusing only on measurements taken during high-concentration dust events, which are presumed to reflect recently emitted aerosols with minimal transport-induced size sorting.

This methodology is implemented here as the 'modified' approach, in which the dispersed soil size distribution from the GMINER SMA is adjusted to more realistically represent the aerosol size distribution observed in atmospheric dust. The formulation follows Perlwitz et al. (2015a), based on BFT. From GMINER, the mass fraction of each mineral k in the conceptual clay (0-2 μm) and silt (2-50 μm) size categories is denoted by $m_k^{\mathrm{c}}(s_{\mathrm{t}})$ and $m_k^{\mathrm{s}}(s_{\mathrm{t}})$, respectively. It should be noted that these two broad categories are used for the mineralogical reallocation process and are distinct from the five discrete aerosol transport bins defined in Table 1. Thse fractions are normalized for each soil type s_{t} (arid soil type provided by FAO74) such that:

$$\sum_{k=1}^{8} m_k^{\mathrm{c}}(s_{\mathrm{t}}) = 1 \text{ and } \sum_{k=1}^{8} m_k^{\mathrm{s}}(s_{\mathrm{t}}) = 1, \tag{10}$$

with 8 minerals considered. To better reflect the emitted PSD, the BFT-based method distributes all minerals across both size categories, including those originally classified exclusively as clay- or silt-sized in GMINER.

To assign mineral fractions to the actual aerosol size categories, soil texture information from the SoilGrids database (Poggio et al., 2021) is incorporated. Let $m^{\mathrm{c}}(s_{\mathrm{x}})$ and $m^{\mathrm{s}}(s_{\mathrm{x}})$ denote the soil mass fractions of clay- and silt-sized particles, normalized such that:

$$m^{\mathrm{c}}(s_{\mathrm{x}}) + m^{\mathrm{s}}(s_{\mathrm{x}}) = 1. \tag{11}$$

The combined soil mineral mass fraction in each size category at each location is then computed by weighting the GMINER mineral fractions by the local soil texture proportions:

$$m_k^{\mathrm{c}}(s_{\mathrm{t}}, s_{\mathrm{x}}) = m^{\mathrm{c}}(s_{\mathrm{x}}) m_k^{\mathrm{c}}(s_{\mathrm{t}}), \quad m_k^{\mathrm{s}}(s_{\mathrm{t}}, s_{\mathrm{x}}) = m^{\mathrm{s}}(s_{\mathrm{x}}) m_k^{\mathrm{s}}(s_{\mathrm{t}}). \tag{12}$$

This ensures that the total soil mineral mass fraction across both reallocation size classes sums to unity:

$$\sum_{k=1}^{8} (m_k^{\mathrm{c}}(s_{\mathrm{t}}, s_{\mathrm{x}}) + m_k^{\mathrm{s}}(s_{\mathrm{t}}, s_{\mathrm{x}})) = 1. \tag{13}$$

In this formulation, soil mineral mass fractions vary spatially according to two factors: the arid soil type (s_{t}), which governs mineralogical composition, and the soil texture class (s_{x}), which determines the relative abundance of clay- and silt-sized particles.

Once the soil mineral fractions are obtained from Eq. (12), the next step is to derive the emitted mass fraction of each mineral in the clay and silt size SMA categories. Denote by ϕ^{c} and ϕ^{s} the total emitted mass fractions of clay- and silt-sized aerosols,

constrained by:

$$\phi^{\mathrm{c}} + \phi^{\mathrm{s}} = 1. \tag{14}$$

These totals are composed of contributions from all minerals k. Let $\phi_{\mathrm{k}}^{\mathrm{c}}$ and $\phi_{\mathrm{k}}^{\mathrm{s}}$ represent the emitted clay- and silt-sized fractions attributable to mineral k. They satisfy:

$$\phi^{\mathrm{c}} = \sum_{k=1}^{8} \phi_k^{\mathrm{c}} \text{ and } \phi^{\mathrm{s}} = \sum_{k=1}^{8} \phi_k^{\mathrm{s}}, \tag{15}$$

and consequently:

$$\sum_{k=1}^{8} (\phi_k^{\mathrm{c}} + \phi_k^{\mathrm{s}}) = 1. \tag{16}$$

Thus, the emitted mineral mass fractions across all species and size classes sum to unity. Following the BFT-based formulation, the global clay-sized emission fraction is prescribed as ϕ^{c}=0.013, constant across all locations. The contribution of mineral k to clay-size emissions is therefore:

$$\phi_k^{\mathrm{c}}(s_{\mathrm{t}}) = \phi^{\mathrm{c}} m_k^{\mathrm{c}}(s_{\mathrm{t}}), \quad \phi^{\mathrm{c}} = 0.013, \tag{17}$$

meaning that the proportion of emitted clay-sized dust mirrors the clay mineral fractions of the fully dispersed soil. In this context, the fully dispersed soil represents a theoretical, maximally dispersed state, a conceptual limit where all aggregates are broken down into their primary, indivisible constituents.

With ϕ^{c} prescribed, the total silt-sized fraction follows implicitly as:

$$\phi^{\mathrm{s}} = 1 - \phi^{\mathrm{c}} = 0.987. \tag{18}$$

For each mineral, the emitted silt-sized fraction $\phi_{\mathrm{k}}^{\mathrm{s}}$ has two sources: (1) particles originally present in the soil in the silt-size range, and (2) primary clay minerals that are emitted within larger silt-sized aggregates during the saltation-driven fragmentation of the parent soil. To account for this, the model performs an empirical reallocation where a fraction of the soil's clay mineral mass is transferred into the silt-sized aerosol population. This is expressed as:

$$\phi_k^{\mathrm{s}} = \vartheta \big(\gamma_k m_k^{\mathrm{c}}(s_{\mathrm{t}}, s_{\mathrm{x}}) + m_k^{\mathrm{s}}(s_{\mathrm{t}}, s_{\mathrm{x}}) \big). \tag{19}$$

where γ_{k} is a mineral-specific reaggregation coefficient quantifying the clay-to-silt transfer, and ϑ is a normalization constant ensuring that the sum of all $\phi_{\mathrm{k}}^{\mathrm{s}}$ equals ϕ^{s}.

For simplicity, γ_{k} is assumed constant across minerals, with the exception of feldspar, gypsum, and quartz. Feldspar is typically overrepresented in the silt fraction due to its fragmentation behavior, while gypsum is soluble and exhibits distinct disaggregation and spatial patterns (Perlwitz et al., 2015a). Quartz, which dominates the coarse end of the size spectrum and shows little evidence of disaggregation, is prescribed with γ_{quartz}=0.

Notably, feldspar and gypsum require special treatment since they are present in both clay and silt fractions of atmospheric aerosols (e.g., Enete, 2012) but are absent from the clay fraction in the GMINER SMA. Consequently, Eq. (17) cannot be applied directly. Instead, their clay-size fractions are estimated following the approach of Gonçalves Ageitos et al. (2023), which uses proxy minerals and scaling ratios: for feldspar, the extension into the clay fraction is scaled according to the quartz clay-to-silt ratio:

$$m^{\mathrm{c}}_{\mathrm{feldspar}}(s_{\mathrm{t}}) = m^{\mathrm{s}}_{\mathrm{feldspar}}(s_{\mathrm{t}}) * \frac{m^{\mathrm{c}}_{\mathrm{quartz}}(s_{\mathrm{t}})}{m^{\mathrm{s}}_{\mathrm{quartz}}(s_{\mathrm{t}})}, \tag{20}$$

and for gypsum, the calcite clay-to-silt ratio is used:

$$m^{\mathrm{c}}_{\mathrm{gypsum}}(s_{\mathrm{t}}) = m^{\mathrm{s}}_{\mathrm{gypsum}}(s_{\mathrm{t}}) * \frac{m^{\mathrm{c}}_{\mathrm{calcite}}(s_{\mathrm{t}})}{m^{\mathrm{s}}_{\mathrm{calcite}}(s_{\mathrm{t}})}. \tag{21}$$

To conserve the total clay-size mass balance (Eq. 10), the phyllosilicate fractions in the clay category are proportionally reduced by soil type.

Once these database gaps are addressed, the emitted silt-sized fraction of mineral k is expressed based on Eqs. (12) and (19) as:

$$\phi^{\mathrm{s}}_{k}(s_{\mathrm{t}}, s_{\mathrm{x}}) = \vartheta(s_{\mathrm{t}}, s_{\mathrm{x}}) \left[\gamma_k m^{\mathrm{c}}(s_{\mathrm{x}}) m^{\mathrm{c}}_{k}(s_{\mathrm{t}}) + m^{\mathrm{s}}(s_{\mathrm{x}}) m^{\mathrm{s}}_{k}(s_{\mathrm{t}})\right]. \tag{22}$$

In this formulation, γ_{k} acts to suppress the silt-size emissions of minerals such as quartz, while extending the contribution of clay-rich species (e.g., phyllosilicates) into the silt range. This redistribution reflects the contrasting aggregation behaviors of different minerals: quartz remains largely intact during saltation, whereas clay-mineral constituents are emitted as part of larger silt-sized aggregates rather than as fully dispersed fine particles.

A schematic representation of the 'modified' approach is shown in the lower panel of Fig. 1. In this framework, a substantial reduction of the quartz fraction is introduced, along with a redistribution of minerals across size classes. Specifically, phyllosilicates are incorporated into the silt fraction, while feldspar and gypsum are extended into the clay fraction. The application of Eqs. (22)–(21) thereby entails a relative decrease of feldspar and gypsum within the silt-size range, resulting from the additional contribution of phyllosilicates.

After constructing the adjusted mineral soil PSD, which better represents the composition of mineral aerosols at larger sizes, it is incorporated into the COSMO5.05-MUSCAT emission scheme. The underlying emission algorithm remains unchanged from the implementation described by Gómez Maqueo Anaya et al. (2024): the vertical emission flux in each MUSCAT size bin is scaled by the corresponding soil mineral fraction, with each mineral assigned to its own bin within the respective size category (see Table 1). In the revised configuration, the mineralogical SMA is updated to reflect the modified PSD, and additional bins are introduced to represent minerals that now occur simultaneously in both clay and silt size ranges.

To verify the 'modified' mineral approach, the scheme was compared against the MONARCH reference for Haplic Xerosols in the northwestern Sahara (Gonçalves Ageitos et al., 2023). Despite differences in bin resolution and emission parameterizations, both models demonstrate a consistent redistribution pattern, specifically, the shifting of phyllosilicates toward silt-sized categories and a proportional reduction in quartz. The resulting mineralogical shift from soil to emitted aerosol for this soil type is illustrated in Fig. B1.

Table 2. Summary of simulations used for measurement comparison. Domain and all input files remain consistent across model runs. For a detailed description of the differences between mineralogy schemes, refer to Section 2.3

Simulation	Time frame	Mineralogy scheme
DUST-CM-01	January-February 2022	'original'
DUST-CM-02	January-February 2022	'modified'
JAT-CM-01	June-July 2022	'original'
JAT-CM-02	June-July 2022	'modified'

2.4 Input files and simulation setup

Mineralogical dust simulations were conducted using a consistent COSMO5.05–MUSCAT physical configuration. The experimental design varied across two primary dimensions: the simulation period and the mineralogical scheme. To match the observational campaigns, simulations were performed for January–February 2022 (DUSTRISK) and June–July 2022 (JATAC). For each of these periods, two distinct mineralogical composition approaches, the 'original' and 'modified' schemes, were applied. The simulation experiments are summarized in Table 2.

The COSMO5.05-MUSCAT model domain is set up to cover the majority of the Sahara Desert and extend westward over the Atlantic Ocean to include the Cape Verde archipelago. The domain is bounded by 30.75°W to 39.32°E and 38.49°N to 0.38°S as represented in Fig. 3. Simulations are conducted at a horizontal resolution of 0.25° (approximately 28 km), with a vertical discretization of 40 layers. The lowest, surface level, model layer has a thickness of 20 m.

Meteorological initial and boundary conditions for COSMO5.05-MUSCAT are provided by the DWD in the form of 3-hourly meteorological fields. To maintain realistic atmospheric conditions, the model is re-initialized every 48 hours using overlapping cycles. Each 48-hour cycle begins with a 24-hour spin-up phase, during which only the COSMO5.05 meteorological model is active. Following this spin-up, MUSCAT is coupled to COSMO5.05 for the remaining 24 hours to simulate aerosol transport and interactions. Only the output from these second-day simulations, when both COSMO5.05 and MUSCAT are fully coupled, is used for analysis. Continuity between cycles is ensured by starting each new COSMO5.05 run 24 hours prior to the end of the previous MUSCAT simulation, while MUSCAT continues using its own prognostic fields from the preceding cycle as initial conditions. The entire simulation period is preceded by a 15 day intial spin-up, and results are outputted at 1 hour intervals.

The MUSCAT dust emission scheme is controlled by external soil-related datasets. Vegetation cover is prescribed using the FCOVER product from the Copernicus Global Land Service (Fuster et al., 2020), which provides fractional green vegetation coverage. Soil moisture input is taken from ERA5-Land hourly reanalysis data (Muñoz Sabater and Copernicus Climate Change Service, 2019), specifically utilizing the volumetric soil water content of the 7 cm uppermost soil layer. Soil texture, expressed in terms of clay, silt, and sand fractions, is provided by the SoilGrids database (Poggio et al., 2021), while aerodynamic roughness lengths are provided through the dataset by Prigent et al. (2005).

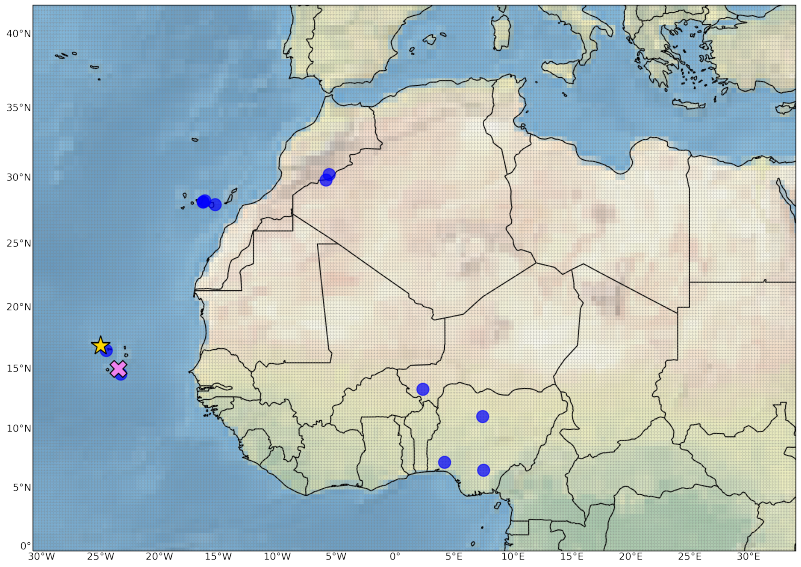

Figure 3. Simulation domain for COSMO5.05-MUSCAT, featuring a 0.25° resolution grid in gray dotted lines. The yellow star identifies São Vicente (Cabo Verde), the site of the JATAC 2022, while the violet X indicates Praia (Santiago, Cabo Verde), where the DUSTRISK 2022 measurements were conducted. Blue dots show the locations of a measurement compilation utilized for a broader model validation.

These datasets, combined with the model's spatial constraints, restrict dust activation exclusively to continental source regions. Furhtermore, the spatial distribution of active dust emission sources is constrained by the MSG-SEVIRI dust source activation frequency map by Schepanski et al. (2007). Finally, the mineralogical composition is represented by the GMINER SMA (Nickovic et al., 2012) implemented via the two distinct modeling approaches detailed in Sect. 2.3.

3 Cape Verde measurement campaigns: in-situ aerosol measurements

3.1 JATAC 2022

During the JATAC 2022 campaign, in-situ recollection of mineral dust aerosols were performed using Unmanned Aerial Vehicles (UAVs) over São Vicente, Cape Verde, (indicated by the yellow star in Fig. 3) throughout June 2022. The Cyprus Institute conducted 25 UAV flights, each equipped with Optical Particle Counters (OPCs) for fine- and coarse-mode height-resolved PSD observations. Dust particles were collected from the atmospheric layers using onboard impactor samples (Marinou et al., 2023), with a Giant Particle Collector (GPaC) capable of capturing particle diameters from nanometers up to tens of micrometers (Kezoudi et al., 2025, 2021). The GPaC's upper size limit depends on airspeed, pressure, and temperature; as a reference, during the SAMUM-2 campaign, particles up to 28.5 µm were successfully collected (Lieke et al., 2011).

Two OPCs were mounted on each UAV. The Universal Cloud and Aerosol Sounding System counted aerosols with diameters from 0.28 to 17.0 µm, while the Printed Optical Particle Spectrometer measured number concentrations in the 0.14–3 µm range

(Kezoudi et al., 2021). OPC measurements were used to validate PSDs derived from collected dust samples, following the methodology of Panta et al. (2023).

Aerosol chemical composition and single-particle characteristics were analyzed using a scanning electron microscope coupled with Scanning Electron Microscope-Energy Dispersive X-ray spectrometry (SEM-EDX) to determine particle size, shape, and elemental composition. Back-scattered images were used to study particles with projected area diameters (PAD) >0.5 μm, where PAD ($D_{\mathrm{p}} = \sqrt{4A_{\mathrm{p}}/\pi}$, with A_{p} as the particle area) closely approximates aerodynamic diameter for dust (Aryasree et al., 2024; Kandler et al., 2018). SEM-EDX provides normalized atomic percentages for elements including: F, Na, Mg, Al, Si, P, S, Cl, K, Ca, Ti, V, Cr, Mn, Fe, Zn, and Pb. This method allows detection of particles up to 30 μm, with measurement precision for major compounds within 2% relative standard deviation (RSD), while minor compounds range from 10–20% for particles >3 μm, and can exceed to 100% for the smallest particles. Diameter measurement uncertainty decreases with size, from ∼1.5% RSD at 2 μm to <1% for particle diameters >3 μm (Kandler et al., 2018).

Impactor sampler collected 18 samples, and analyzed size, shape and elemental composition for 25000 single particles during the measurement period. Samples with a low number of particles (<500) were discarded to ensure reliable statistics while counting/grouping each particle group. This screening protocol resulted in a final validation dataset comprising 17 high-quality samples.

In this study, one of the main objectives is to accurately represent the aerosol dust mineralogy in future modeling studies using measurement data. Hence, we adopt a classification scheme for mineral dust aerosols representative of the soil database as used in the model. Size-segregated (same as Table 1) chemical composition of major dust aerosols: illite, kaolinite, smectite, quartz, feldspar, calcite, gypsum and hematite were derived by defining ideal elemental compositions for the modeled minerals in the elemental space. The used composition in terms of mass compositions are shown in Table A. This classification scheme assigns the single particles to the closest ideal composition. Counting statistics for each particle group are used to estimate uncertainty by generating two-sided 95% confidence intervals under a binomial assumption.

For iron oxide minerals such as hematite, the ratio reported in Table A reflects the iron oxide content from a single-particle perspective. However, a significant fraction of iron in dust occurs within the crystal lattice of other minerals (Lafon et al., 2004; Zhang et al., 2015), necessitating an alternative approach to estimate total iron oxide content.

Following Aryasree et al. (2024), we use two parameters: (i) the total iron oxide percentage (Fe_{oxides}), which accounts for iron present either as pure oxy-hydroxides (e.g., hematite, goethite) or incorporated within mineral lattices, and (ii) the total Fe index, defined as the atomic ratio of Fe to the sum of all quantified elements. The total iron oxide percentage is calculated as:

$$Fe_{\mathrm{oxides}} = \left(\frac{m_{\mathrm{Feox\%}}}{m_{\mathrm{Fe\%}}}\right) * \left(\frac{M_{\mathrm{Fe}}}{M_{\mathrm{dry}}}\right) * 100, \tag{23}$$

where $m_{\mathrm{Feox\%}}$ and $m_{\mathrm{Fe\%}}$ are the mass fractions of iron oxides and elemental iron relative to the total dust mass, respectively, obtained from Table 3 in Di Biagio et al. (2019) for different Saharan source regions. M_{Fe} is the estimated Fe mass within a single particle from SEM-EDX measurements, and M_{dry} is the particle's dry mass.

Using this formulation, mass percentages for both total iron oxide and hematite are derived. For hematite specifically, hematite mass fraction from Di Biagio et al. (2019) is used to substitute $m_{\mathrm{Feox\%}}$ in Eq. (23). The uncertainty arising from the representative

ratio of iron oxide content from 19 desert dust types given by Table 3 in Di Biagio et al. (2019) which is generally less than 15%. For us, this is a systematic error, as we apply the same ratio to all samples.

Additionally, elemental mass concentrations are provided for the species most commonly associated with mineral dust, including Si, Al, Fe, Ca, K, Mg and S. Both mineralogical and elemental data are partitioned into the MUSCAT size bins up to BIN26.

3.2 DUSTRISK 2022 campaign

The DUSTRISK 2022 campaign took place in the Cape Verde archipelago during January and February 2022. Particulate matter was sampled at two distinct sites, referred to as inflow and outflow, on the island of Santiago (Cabo Verde). The inflow site (14°54'32" N, 23°30'54" W, indicated by the violet X in Fig. 3) was positioned in the city of Praia, on the northeastern coast, directly facing the ocean.

The sampling site was strategically positioned to intercept air masses dominated by the prevailing northeast trade winds, which transport Saharan mineral dust directly from the African continent. Located upwind of both the urban center of Praia and the island's interior, the site is well-situated to ensure that collected aerosols represent long-range continental transport with minimal interference from local island soils. Although minor anthropogenic contributions from nearby urban areas cannot be entirely discounted, the site's orientation ensures that local influences remain negligible, as corroborated by previous studies (Cardoso et al., 2018; Fomba et al., 2025). In contrast, the outflow site is positioned downwind of the major metropolitan area and is significantly more susceptible to local anthropogenic and local dust emissions (Bredeck et al., 2024; Souza et al., 2025). To ensure direct comparability with model simulations that represent only continental dust sources, this analysis focuses exclusively on measurements from the inflow site.

Particulate matter (PM) samples were collected using Digitel DHA-80 high-volume samplers (Walter Riemer Mess Technik, Germany) operating at an average flow rate of 500 L min^{-1}. At each site, separate $PM2.5$ and $PM10$ samplers were deployed. Sampling typically occurred over 24-hour periods (noon to noon); however, during pronounced dust events, sampling duration was shortened to capture peak concentrations. All samples were collected on Ahlstrom micro-quartz fiber filters (MK 360) (Bredeck et al., 2024; Souza et al., 2025).

Elemental concentrations were determined using Total reflection X-Ray Fluorescence (TXRF) spectroscopy, following the methodology described by Fomba et al. (2020). Filter samples of 1.5 cm^2 area were prepared by digesting three 8 mm spots per filter in a HCl/HNO_3 mixture (0.375 mL and 1.125 mL, respectively) using a microwave digester (Mars 6, CEM, Germany). Internal standards (Sc/Co at 10 μL) were added to the digested solutions, which were then applied to siliconized quartz carriers, dried at 80°C, and analyzed using a Bruker S4 T-STAR instrument. This procedure determined concentrations of Al, Ti, Ca, K, Mg, S, Si, Cr, Mn, and Fe. To ensure precision and account for potential sample heterogeneity, each carrier was analyzed at two rotational positions (0° and 90°). Measurement uncertainty was quantified by calculating the relative error between these replicates, revealing a dependency on mass loading: uncertainties reached up to 15% for samples with very high dust load (> 150 $\mu g/m^3$) while remaining below 6% for samples with low dust concentrations typically below 38 $\mu g/m^3$. These variations are attributed to instrumental limitations previously characterized in (Fomba et al., 2020).

Notably, blank silicon measurements for the filters and TXRF sample carriers showed significant, non-reproducible variations due to inconsistent filter densities and surface reflectance. The resulting uncertainties were too high for a meaningful comparison; therefore, silicon was excluded from the analysis. To isolate the mineral dust signal from the background aerosol, the total mineral dust mass concentration was reconstructed from the remaining elemental data following the procedure of Souza et al. (2025). In this approach, the concentrations of key crustal elements (Al, Fe, Ca, Ti) are adjusted for their common oxide forms to estimate the total mineral mass. The dust concentrations were quantified using the stoichiometric relationship for crustal elements following Deabji et al. (2021); Souza et al. (2025):

$$\mathrm{MD} = 1.16 \times ((1.90 \times \mathrm{Al}) + (23.3 \times \mathrm{Ca}) + (2.09 \times \mathrm{Fe}) + (1.67 \times \mathrm{Ti})) . \tag{24}$$

Following established classification for mineral dust events in the Cabo Verde region (Souza et al., 2025), a mineral dust mass concentration threshold of $\geq$38 $\mu g/m^3$ was applied. The threshold was chosen based on long-term analysis of PM10 concentrations at the CVAO sampling site, during which dust concentrations were consistently high. This threshold, combined with air mass back-trajectory analysis, serves to distinguish significant long-range transported dust events from maritime background or localized aerosols. This screening resulted in a final validation set consisting of 33 PM2.5 and 47 PM10 filter samples.

4 Model comparison framework

4.1 Evaluation methodology

To ensure a robust comparison between COSMO5.05-MUSCAT simulations and in-situ observations, the model output is spatio-temporally sampled to align with the specific characteristics of each measurement campaign. Spatially, model variables were extracted from the grid cells corresponding to the geographic coordinates of the sampling sites. Temporally, hourly model outputs were averaged over the specific integration times of the filter samples. This alignment accounts for varying sampling durations, ranging from the high-frequency UAV cycles during JATAC 2022 to the day-long ground-based periods of the DUSTRISK 2022 campaign. To ensure temporal concurrency, a rounding convention is applied: if a sampling interval began or ended within 30 minutes of a full hour, the nearest hourly model timestep is used to define the averaging window. For example, a sampling period from 10:00 to 12:15 is matched with the model average from 10:00 to 12:00, while a period from 10:10 to 12:36 is matched with the 10:00 to 13:00 simulated average.

For the compilation of North African mineralogical measurements, where exact temporal matching is often not possible due to the lack of concurrent simulated data, the time dimension is constrained by selecting observations from the same seasons as the simulation period. Furthermore, the comparison is restricted to sites and dust trajectories similar to those simulated, ensuring that the emission sites to measurement place pathways in the model are representative of the taken measurements, as detailed in the following section.

It is important to note that the ‘original’ mineralogy scheme (Gómez Maqueo Anaya et al., 2024) possesses structural constraints regarding the simulation-to-measurements comparisons. Specifically, phyllosilicates are restricted to the clay and

fine-silt fractions (BIN01 and 1/2 BIN03), while minerals such as feldspar and gypsum are defined with no mass in the clay-sized fraction (BIN01). These inherent model configurations limit the scope of certain comparisons where observations report these minerals in size fractions not supported by the scheme's internal mapping.

The agreement between simulated (S) and observed (O) mineralogical and elemental concentrations is quantified using the Mean Bias (MB) and the Pearson correlation coefficient (r). In this framework, r is utilized as a measure of spatial correlation to evaluate the model's ability to replicate the geographical variability and regional distribution of mineral dust signatures across the study domain. The Pearson correlation coefficient is defined as:

$$r = \frac{\sum_{i=1}^{n}(S_i - \bar{S})(O_i - \bar{O})}{\sqrt{\sum_{i=1}^{n}(S_i - \bar{S})^2 \sum_{i=1}^{n}(O_i - \bar{O})^2}}, \tag{25}$$

where $\bar{S}$ and $\bar{O}$ represent the mean values of the simulated and observed datasets, respectively, and n is the number of paired spatial samples. Complementary to this, the Mean Bias (MB) identifies systematic over- or underestimations and is calculated as:

$$MB = \frac{1}{n}\sum_{i=1}^{n}(S_i - O_i). \tag{26}$$

4.2 Compilation of North Africa mineralogical measurements

To evaluate the improvements introduced by the 'modified' mineralogy scheme, we compared the DUST-CM-01 and DUST-CM-02 model outputs (see Table 2 for the list of the model experiments) against a compilation of in-situ aerosol mineralogical measurements. This simulated period (January-February 2022) was specifically selected to facilitate a direct comparison with the 'original' mineralogy scheme presented by Gómez Maqueo Anaya et al. (2024). By maintaining this temporal window, we ensure that differences in model performance are attributable to the updated mineralogical parametrization rather than variations in meteorological forcing across different years.

The core of this compilation is based on the global dataset of Perlwitz et al. (2015b). As an initial step, the primary global datasets were subset to include only locations within the modeling domain. The subsequent systematic processing is illustrated in Figure 4, which delineates the pathways for both in-situ observations (gray arrows) and COSMO5.05-MUSCAT simulation results (green arrows). The datasets from both observations and modeling results are represented by yellow boxes with slanted corners. Following the observational pathway, the data undergoes a seasonal filter to retain only measurements representative of Northern Hemisphere (NH) winter months. This step, represented by the first blue hexagon (decision point) in Figure 4, ensures the observational dataset closely matches the simulation period.

This seasonal constraint is critical, as Saharan dust emissions and transport pathways exhibit pronounced intra-annual variability (Barkan et al., 2004; Schepanski et al., 2009). Specifically, different dust source regions are active during NH winter versus summer, resulting in distinct mineralogical signatures at the receptor sites. By restricting the compilation to the NH winter season, we ensure that the dust sources activated within the model's simulation are representative for the measurement comparison.

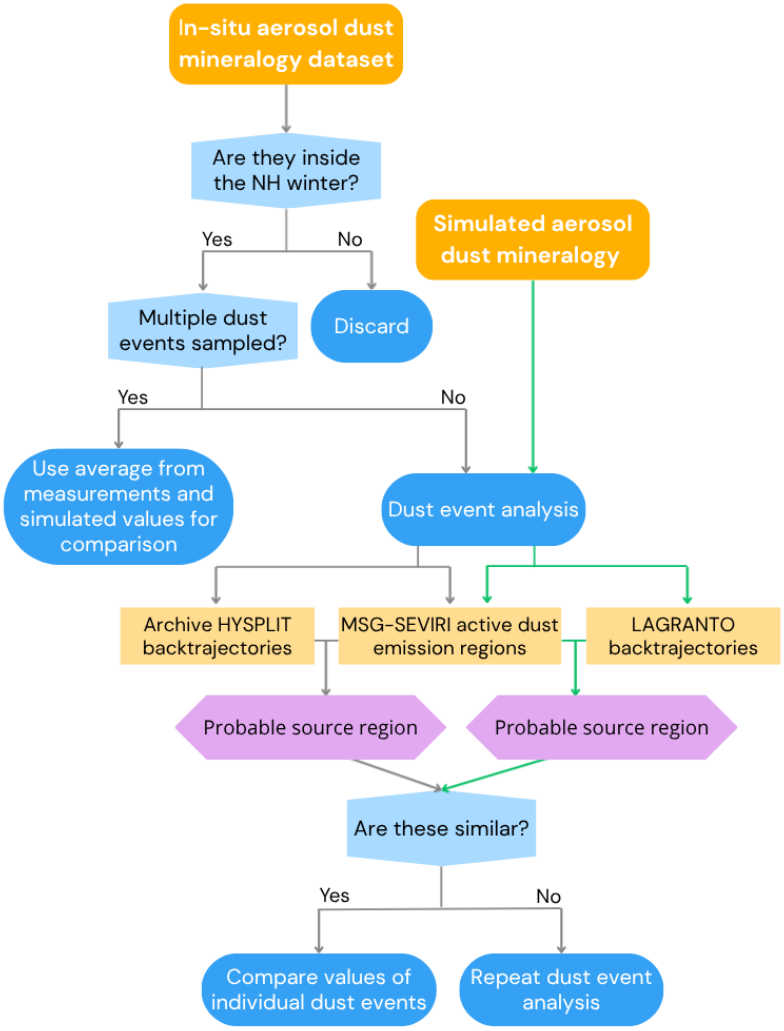

Figure 4. Schematic representation of the workflow used to select and compare in-situ mineral dust measurements with COSMO5.05-MUSCAT simulations. Primary datasets are displayed in yellow boxes with slanted corners and bold text. The analysis pathway for simulated mineralogy is depicted by green lines and arrows, while the in-situ measurement selection process is indicated by gray lines and arrows. Decision points are represented by blue hexagons, procedural steps by blue octagons, supplementary datasets by yellow rectangular boxes, and final outcomes by lavender octagons.

The second decision point in Fig. 4 determines the specific simulation data utilized for the comparison based on the number of dust events captured. Measuring campaigns that sampled more than two distinct dust events are categorized as long-term campaigns. For these cases, average mineral mass fractions for the measurement locations grid cell are computed over the entire DUST-CM's simulation period and compared directly against the observed measurements. This approach was applied to the datasets of Adedokun et al. (1989); Enete (2012); Formenti et al. (2008); Kandler et al. (2009, 2011); Møberg et al. (1991) and Panta et al. (2023).

In contrast, shorter campaigns covering two or fewer dust events required a more detailed matching procedure, initiating the "dust event analysis" workflow illustrated in Fig. 4. This methodology integrates HYSPLIT back trajectories (Stein et al., 2015) with satellite-derived dust emission records from the MSG-SEVIRI Dust RGB product (EUMETSAT) to identify probable source regions, following the approach of Schepanski et al. (2007), recently applied in Souza et al. (2025).

To ensure a like-to-like comparison, simulated dust plumes were selected only when their transport pathways and source regions were consistent with the specific observed events. For these cases, the comparison was performed using model output extracted from the grid cell corresponding to the geographic coordinates of the measurement site. The "dust event analysis" workflow, illustrated in Figure 4, begins by identifying the probable source region of the observed sample using HYSPLIT back-trajectories (Stein et al., 2015) intersected with dust emission records from the MSG-SEVIRI Dust RGB product. Simultaneously, backward trajectories for simulated dust events were computed using the LAGRANTO tool (Miltenberger et al., 2013), driven by COSMO5.05 meteorological fields. Comparison with measurements proceeded only when the simulated and observed plumes originated from the same dust source region, thereby allowing for the direct matching of individual plume signatures with high-resolution model outputs.

Three campaigns required this rigorous event-based matching procedure: Alastuey et al. (2005), Jeong and Achterberg (2014), and Kandler et al. (2007). For Alastuey et al. (2005), which predates the MSG-SEVIRI record, Meteosat-7 natural color imagery was utilized to track the specific plume transported from southern Algeria to Tenerife on 29 July 2002. For the remaining campaigns, observed plumes were individually matched to simulated events by ensuring that both the HYSPLIT (observational) and LAGRANTO (model) back-trajectories intersected with the same active MSG-SEVIRI dust emission areas.

The final dataset was further expanded with additional North African measurements not considered in the original Perlwitz et al. (2015b) compilation. This expanded dataset is publicly available via the zenodo repository (https://doi.org/10.5281/zenodo.19731364), and the corresponding measurement locations are represented by blue dots in Fig. 3. It should be noted that several historical measurements from the 1970s included in the Perlwitz et al. (2015b) study could not be reliably traced using this meteorological and satellite-based framework; consequently, these samples were excluded from the comparison to maintain the integrity of the spatio-temporal matching.

To ensure a robust comparison between varying measurement techniques and model outputs, size-matching was performed based on the reported diameter ranges. For each comparison, the simulated mineral mass fraction was calculated by integrating the mass of a specific mineral across the relevant model bins and dividing this sum by the total simulated dust mass within those same bins. For campaigns reporting bulk measurements, model values were integrated across all available size bins (BIN01 through BIN80). For measurements classified as "clay," the mass fraction was derived from BIN01 + 1/2 BIN03, while

"silt" classifications were compared to the average of 1/2 BIN03 + BIN09 + BIN26 + BIN80. For the campaign reporting high-resolution size distributions (Panta et al., 2023), model bins were matched to the closest reported diameter ranges: 0—1 µm is compared to BIN01; 1—2 µm to BIN03; 4—8 µm to BIN09; 8—16 µm to BIN26; and 32—64 µm to BIN80.

Following these spatio-temporal and size-matching constraints, the final mineral mass fraction comparison is performed using the model output from the specific grid cell corresponding to each measurement site. While measurement uncertainties were not consistently reported across all original studies, they have been included in the comparison with simulated data whenever available.

Despite these rigorous criteria, inherent uncertainties remain. Meteorological anomalies or atypical seasonal transport patterns in the historical data may not be fully captured by the January–February 2022 simulation period. Furthermore, several sites are located near major dust sources where local emissions may dominate the observed mineralogy in ways the model's spatial resolution cannot fully resolve (e.g., Formenti et al., 2008; Kandler et al., 2009; Møberg et al., 1991; Panta et al., 2023).

Finally, inconsistencies in particle size classification across datasets, such as varying definitions for "bulk," "clay," and "silt" fractions, introduce additional uncertainty. While model bins were mapped to these categories as previously described, the sensitivity of these boundaries (e.g., 2.0 vs 2.5 µm) highlights the necessity for high-resolution, well-characterized, and concurrent datasets, such as those obtained during the DUSTRISK 2022 and JATAC 2022 campaigns.

4.3 Application to Cape Verde measurement campaigns

4.3.1 Mineralogy comparison

Within the Cape Verde campaigns, mineralogical measurements were exclusively available from the JATAC 2022 dataset. For this evaluation, simulated mineral mass fractions from the JAT-CM-01 and JAT-CM-02 experiments were compared against the in-situ observations by extracting model variables from the grid cells corresponding to São Vicente. To ensure temporal and vertical alignment, the model output is averaged over the specific sampling intervals and the documented altitude ranges of the UAV flights.

In terms of particle size, the JATAC 2022 observations are inherently compatible with the MUSCAT bin definitions, requiring no additional size-matching adjustments. However, BIN80 (32–64 µm) is excluded from the assessment due to the analytical detection limits of the substrate composition methodology (see Sec. 3). Consequently, each specific mineral mass fractions measurements from the validated samples are directly matched to its corresponding simulated mass fraction to evaluate the model's mineralogical representation.

4.3.2 Elemental comparison

Elemental compositions were evaluated for both the DUSTRISK and JATAC 2022 campaigns. To facilitate a direct comparison with the filter-based measurements, simulated mineral mass concentrations were converted into elemental mass fractions using the stoichiometric percentages defined in Table 3. For each specific element, the total simulated mass is calculated by summing the contributions from all relevant minerals, which is then normalized by the total simulated dust mass to yield an elemental mass

Table 3. Mass percentage of key elements found in the COSMO5.05-MUSCAT simulated minerals. The smectite group is represented by the end-member montmorillonite, and feldspar is represented by a 1:1 average of microcline (K-feldspar) and albite (Na-feldspar). This selection is based on common mineralogical assemblages observed in Saharan dust aerosols (Scheuvens et al., 2013; Formenti et al., 2011, 2014).

Mineral	**Fe** [%]	**Si** [%]	**Al** [%]	**Mg** [%]	**K** [%]	**Ca** [%]	**S** [%]
Hematite	69.94	-	-	-	-	-	-
Illite	1.43	25.25	9.01	1.87	6.03	-	-
Kaolinite	-	21.76	20.90	-	-	-	-
Smectite	-	20.46	9.83	-	-	0.73	-
Quartz	-	46.80	-	-	-	-	-
Feldspar	-	30.89	10.23	-	14.05	0.76	-
Gypsum	-	-	-	-	-	23.28	18.62
Calcite	-	-	-	-	-	40.04	-

fraction. We focus our analysis on Fe, Si, Al, Mg, K, Ca, and S, as these elements serve as key tracers for mineral identification and source attribution in Saharan dust studies (Kandler et al., 2018; Formenti et al., 2011; Panta et al., 2023).

It should be noted that certain mineral groups, specifically feldspar and smectite, exhibit significant natural variability in their elemental ratios. For this study, the stoichiometric coefficients for these species were selected to reflect the chemical signatures most commonly observed in the North African and Saharan regions (e.g., Kandler et al., 2007; Formenti et al., 2014; Scheuvens et al., 2013). The spatio-temporal extraction followed the protocols described in Section 4, with size-matching adjusted according to the specific sampling characteristics of each campaign:

- **DUSTRISK:** Observational elemental masses from inflow sites were normalized by the total measured mass. To match the reported size fractions, model outputs were aggregated into PM2.5 (BIN01 + 1/2 BIN03) and PM10 (BIN01 + BIN03 + BIN09).
- **JATAC:** No size-matching adjustments were required, as the measurement characteristics align directly with the MUSCAT bin definitions.

5 Model validation

5.1 Mineralogy

To evaluate the performance of the 'modified' mineralogical scheme, we compare the simulated dust composition against two distinct observational benchmarks. First, we assess the model's ability to capture the general characteristics of North African mineral dust using a comprehensive compilation of historical aerosol measurements from across the region. This provides a statistically robust baseline for regional performance. Second, we evaluate the scheme's precision during a specific transport

Table 4. Mean bias (MB) of the mineral mass fractions for the 'original' (DUST-CM-01) and 'modified' (DUST-CM-02) schemes. The MB is calculated against the North African measurement compilation. The number of observation points used for each comparison is indicated in the parentheses (n).

Mineral	MB [%] (n)	
	DUST-CM-01	**DUST-CM-02**
illite	4.3 (9)	9.4 (13)
kaolinite	-5 (12)	1.2 (17)
feldspar	-0.1 (11)	-5.3 (13)
calcite	-1.9 (16)	-2.4 (16)
hematite	-0.2 (9)	-0.2 (9)
quartz	27.4 (21)	1.8 (21)

event using high-resolution mineralogical data from the JATAC 2022 campaign. Together, these comparisons offer a multi-scale validation of the model's capacity to represent both climatological means and episodic variability in dust mineralogy.

5.1.1 Compilation of North Africa aerosol mineralogical measurements

Two simulations were performed for the DUSTRISK 2022 period to assess the 'original' and 'modified' schemes (DUST-CM-01 and DUST-CM-02, respectively). These runs are compared with historical North African observations from locations and seasons with consistent transport pathways (Section 4.2). Performance metrics, including mean bias and spatial correlations, are synthesized in Table 4 and Fig. 5 (where yellow stars denote the 'modified' scheme). Error bars in Fig. 5 represent the observational uncertainties when reported in the original experimental studies.

The differences between the two simulations are consistent with the structural changes described for the 'modified' approach. Comparing the two simulations directly, the transition from the 'original' to the 'modified' approach results in a fundamental redistribution of mass among the mineral species. Specifically, DUST-CM-02 produces higher mass fractions for illite and kaolinite and lower mass fractions for quartz and feldspar compared to the DUST-CM-01 run.

When evaluated against the North African measurement compilation (Fig. 5), the redistribution of mineral mass in DUST-CM-02 leads to varying impacts on model skill. The most significant improvements are observed for kaolinite, where increased simulated mass fractions reduce the systematic underestimation seen for the DUST-CM-01 run. As shown in Table 4, kaolinite shifts from an underestimation (-5%) to a slight overrepresentation (+1.2%), while also being the only mineral to show a clear improvement in spatial correlation (r_{p}). While illite exhibits a marginal correlation improvement, its overestimation is amplified in DUST-CM-02. This discrepancy is partly attributed to the broad mineralogical definition of illite groups, which complicates unique identification (Rieder et al., 1998, and references therein). Notably, however, illite remains the only mineral species among those compared to demonstrate a moderate spatial correlation.

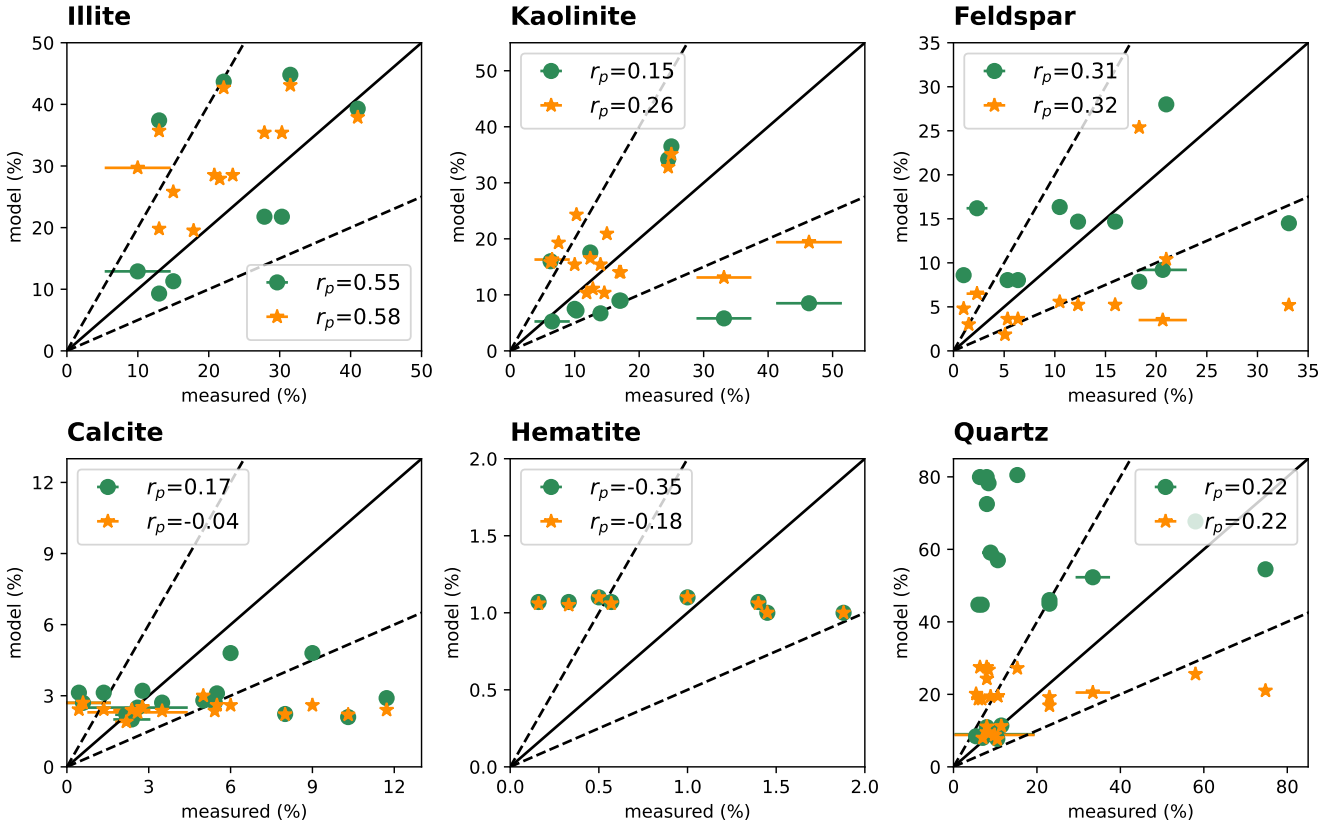

Figure 5. Scatterplots of mineral mass percentages of illite, kaolinite, feldspar, calcite, hematite and quartz measured vs. simulated values. Results from the 'original' simulation (DUST-CM-01) are shown as green solid dots, while the 'modified' approach (DUST-CM-02) is illustrated by yellow solid stars. The dashed lines represent the 1:2 and 2:1 ratios between simulated and observed values. Error bars indicate observational uncertainties as reported in the original studies; where no error bars are present, uncertainties were not provided in the source data. The comparison includes both bulk and size-segregated measurements, with model bins aggregated to match reported diameter ranges as detailed in Section 4.2. Pearson correlation coefficients (r_{p}.) for each approach are shown in the legend.

Regarding the non-phyllosilicates minerals, quartz shows the most striking quantitative improvement; its MB is reduced from a $\sim$30% overestimation in the 'original' scheme to only 1.8% in the 'modified' version, significantly enhancing overall model-observation agreement. Conversely, while the DUST-CM-02 run improves the evaluation scope by including feldspar in the finest size fraction (Eq. 20), a 49% reduction in its simulated mass exacerbates the existing model-observation discrepancy, leading to a larger negative MB (Table 4).

Despite these shifts in mass loading, the spatial correlations (r_{p}) for both quartz and feldspar remain largely unaffected between the two modeling approaches. This stability suggest that for r_{p}, even though the underlying soil mineralogy distribution changed, the transport patterns remain similar enough to not enact changes on it. Moreover, the impact of the DUST-CM-02

scheme on correlation is evident when considering the expanded observational scope. For illite and kaolinite, the inclusion of previously unrepresented size fractions allowed for a more comprehensive validation against a larger pool of data points (Table 4), resulting in a notable and positive shift in r_{p}. While a similar size-range expansion was applied to feldspar, the addition of two observational points was insufficient to yield a statistically significant change in its correlation.

The representation of calcite and hematite remains a challenge. Despite moderate increases in their simulated mass fractions (12% and 17%, respectively from DUST-CM-01 to DUST-CM-02), calcite remains underestimated ($MB \simeq$-2%) and hematite correlations remain poor with negative r_{p} values. Interestingly, for the same number of observation points, the two minerals showed diverging trends in spatial skill: hematite r_{p} improved from -0.35 to -0.18, while calcite correlation degraded from 0.17 to -0.04. The shift in hematite suggests that the mass redistribution in DUST-CM-02 partially corrected previous spatial mismatches, making the model "less wrong" regarding its distribution, even if a negative correlation persists. These discrepancies likely stem from inherent uncertainties in hematite quantification, which occurs both as discrete particles and within other mineral lattices (Lafon et al., 2004; Zhang et al., 2015). Furthermore, the fact that these domain averaged mass increases are not strongly reflected in the site-specific comparisons of Fig. 5 suggest that the modified mass allocation may have introduced new spatial biases by reducing calcite particles which could result in an incorrect emission calculation for this mineral.

Potential biases in the measurement dataset should also be considered. For instance, the inclusion of the FRAGMENT campaign added $\sim$40% more data to the reference set (Fig. 5 in Gómez Maqueo Anaya et al. (2024)). These measurements, reported by Panta et al. (2023), were collected in the Drâa Valley, Morocco, near active dust source regions. Such localized influences may not be captured by the model, as its 28 km spatial resolution represents grid-cell averages and does not resolve small-scale convective events. Likewise, several other campaigns included in the comparison were conducted close to dust sources, reflecting local emissions rather than regional transport observations. Consequentially, these point observations may not fully represent the broader mineral fraction distributions that the model is designed to simulate. Seasonal coverage also plays a role: while some campaigns spanned transitional months with shifts in dominant source regions, the simulations are restricted to NH winter (January–February), potentially missing these seasonal variations (Gebauer et al., 2026). Ultimately, while the scale mismatch between point measurement and grid-cell average persists, the DUST-CM-02 framework provides a more robust baseline for mineralogical validation. By identifying where temporal and spatial representativeness limit our correlations, this approach clarifies the specific observational constraints needed to further reduce uncertainty in mineral dust modeling.

5.1.2 Comparison with JATAC 2022

The comparison between in-situ mineral dust aerosol measurements from the JATAC 2022 campaign and COSMO5.05-MUSCAT simulations is illustrated across several figures: Fig. 6 presents results for individual and grouped phyllosilicates (labeled as “clay minerals”), while Fig. 7 show the comparisons for quartz, calcite, feldspar and gypsum and Fig. 8 show the comparison for hematite. For this evaluation, we contrast the ‘original’ mineralogical scheme (JAT-CM-01; Gómez Maqueo Anaya et al., 2024) with the ‘modified’ approach (JAT-CM-02; Sect. 2.3). As detailed in the evaluation methodology (Sect. 4.3), measurements were binned to match the COSMO5.05-MUSCAT size categories (BIN01 through BIN26).

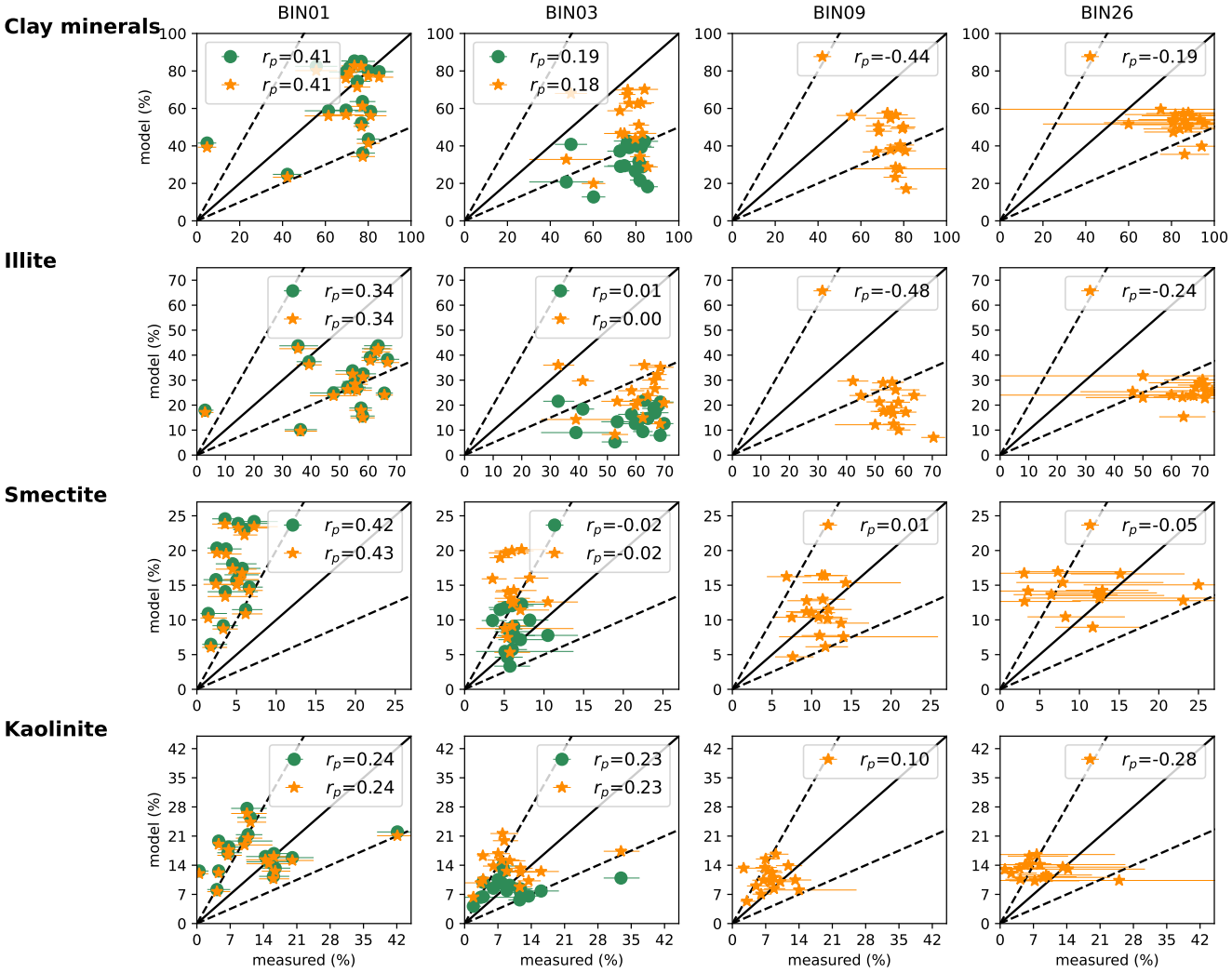

Figure 6. Scatterplots of minerals mass percentages of the grouped "clay minerals", illite, smectite, and kaolinite vs. simulated by COSMO5.05-MUSCAT. 'original' mineral emission scheme (JAT-CM-01) in green solid dots while the 'modified' version (JAT-CM-02) is shown in yellow solid stars. The titles of the columns are size classifications from COSMO5.05-MUSCAT, the diameter ranges they represent are described in Table 1. The dashed lines represent the ratios of 2:1 and 1:2 between the simulated and observed mineral percentages. The error bars represent the lower and upper limits of the confidence intervals (between 2.5% and 97.5%).

Table 5. Mean bias (MB) of the mineral mass fractions for the 'original' (JAT-CM-01) and 'modified' (JAT-CM-02) schemes. The MB is calculated against the JATAC 2022 mineral measurements. The number of observation points used for each comparison is indicated in the parentheses (n).

Mineral	MB [%] (n)							
	JAT-CM-01				JAT-CM-02			
	BIN01	BIN03	BIN09	BIN26	BIN01	BIN03	BIN09	BIN26
clay minerals	-4.2 (17)	-42.2 (17)	–	–	-6.7 (17)	-23 (17)	-32.4 (17)	-32.8 (17)
illite	-21.6 (17)	-43.7 (17)	–	–	-22.6 (17)	-34.5 (17)	-35.8 (17)	-42.2 (17)
smectite	12.5 (17)	2.3 (17)	–	–	11.8 (17)	7.5 (17)	0.3 (17)	2.9 (15)
kaolinite	4.9 (17)	-1.2 (17)	–	–	4.1 (17)	3.9 (17)	3 (17)	4.5 (16)
quartz	1.6 (17)	25.2 (17)	46.1 (17)	62.3 (14)	1.6 (17)	6.7 (17)	9.2 (17)	15.7 (14)
calcite	-1.6 (17)	-4 (17)	-4.2 (18)	1.1 (9)	-1.6 (17)	-4.3 (17)	-4.8 (17)	0.5 (9)
feldspar	–	2.5 (17)	9.9 (17)	14.3 (15)	-1.9 (17)	-1.3 (17)	0.3 (17)	2.2 (15)
gypsum	–	-6.3 (17)	-2.7 (17)	-3.2 (14)	-7.8 (17)	-6.2 (17)	-3.3 (17)	-4 (14)
hematite	-0.9 (17)	-0.5 (17)	-0.1 (17)	0.1 (17)	-0.9 (17)	-0.4 (17)	0.1 (17)	0.1 (17)

For the grouped phyllosilicates in Fig. 6, the model generally underestimating the total mass fraction across all size ranges. A key functional improvement of the 'modified' scheme (JAT-CM-02) is the redistribution of these minerals into coarser size bins, enabling a direct comparison beyond the sub-2.5 µm fraction where the 'original' scheme was restricted and therefore no direct comparison between schemes can be made. In the finest fraction (BIN01), both approaches show a similar underrepresentation with MB values of -4.2% for JAT-CM-01 and -6.7% for JAT-CM-02. However, in BIN03, JAT-CM-02 reduces the underestimation by half compared to JAT-CM-01, suggesting that the 'modified' scheme more accurately captures the mass distribution in coarser fractions. Within the expanded comparison size range, the model underestimation remains consistent across both coarse size bins (Table 5). Notably, the highest spatial correlations (r_{p}) for the phyllosilicates grouped comparison are moderate and found in BIN01, showing little sensitivity to the structural differences between the two schemes (Fig. 6).

Regarding individual species, measured illite fractions during JATAC 2022 were notably high, falling above the typical ranges in the North African compilation (Fig. 5). This localized observational trend leads to a systematic underestimation in both model versions. Such discrepancies partly reflects the known challenges in identifying these specific mineral groups in SEM-EDX measurements (Rieder et al., 1998), introducing uncertainties in both the observations and the reference mineralogical databases. The Pearson correlation coefficient (r_{p}) remain insensitive to the choice of scheme, with the strongest correlations and lowest mean biases occurring in BIN01. While JAT-CM-02 reduces the bias for BIN03, significant underestimation persists and scales with increasing particle size (Fig. 6 and Table 5).

Conversely, smectite and kaolinite are generally overestimated across the simulations. Both minerals show a performance improvement under JAT-CM-02 in terms of reduced mean biases for BIN01. JAT-CM-02 further exacerbates the overestimation in the coarser BIN03: for kaolinite, it shifts a slight underestimation toward a more pronounced overestimation, while for smectite, the overestimation grows. Among the individual phyllosilicates, the strongest r_p values are consistently found in BIN01, regardless of the scheme employed. While kaolinite exhibits weak but stable correlations across both BIN01 and BIN03, spatial correlations for the coarser sizes of both minerals remain weak or negative (Fig. 6 and Table 5).

As expected, the grouped phyllosilicate category exhibits r_p values similar to those of the individual species, as this metric is inherently tied to the mineral distribution within the parent soil. Notably, nearly all spatial correlations for the coarser size bins are negative. This suggests that shifts in the mineral PSD do not necessarily align with the composition of the parent soil. Such statistical decoupling is significant, given that illite and kaolinite distributions vary distinctly across the North African desert (Formenti et al., 2008, 2014; Scheuvens et al., 2013). This discrepancy may stem from uncertainties in the source maps that define these regional signatures. Alternatively, it may arise from the methodological assumption that phyllosilicates identified in the clay-sized fraction via wet-sieving are similarly present in coarser fractions, despite being undetectable by those specific measurement techniques.

These findings build upon the work of Gonçalves Ageitos et al. (2023) who noted that the GMINER SMA (Nickovic et al., 2012) generally outperforms Journet et al. (2014) SMA in reproducing the spatial distribution of phyllosilicates, despite a tendency to overestimate kaolinite and smectite while underestimating illite across the Sahara. Their analysis further showed that for fine clay-sized fractions, illite is often overestimated near sources but underestimated during long-range transport, whereas coarser silt-sized illite is typically underestimated. Our comparison with JATAC 2022 measurements corroborates these trends, showing a persistent underestimation of illite across all simulated size bins. This suggests that while the JAT-CM-02 mass redistribution aims for greater accuracy, it may be amplifying existing uncertainties inherent in regional phyllosilicates source functions.

For the non-phyllosilicates minerals shown in Fig. 7, the JAT-CM-02 run significantly reduces quartz overestimation, particularly from BIN03 onward. Mean biases decrease from 25.2%, 46.1%, and 62.3% in the JAT-CM-01 run for BIN03, BIN09, and BIN26, respectively, to 6.7%, 9.2% and 15.7% in JAT-CM-02 (Table 5). Despite these substantial quantitative improvements, overestimations remain high relative to measured values, and the spatial correlations (r_p) exhibit high variability across size bins. Similar to the phyllosilicate results, the two smallest size fractions show no difference between modeling schemes, maintaining weak but consistent correlations. In contrast, the correlation for BIN09 improves under JAT-CM-02, though it remains statistically insignificant, while the correlation for BIN26 worsens (Fig. 7). The sharp decline in quartz correlation for the coarsest fraction (BIN26), likely results from the significant reduction in simulated coarse-mode mass in the JAT-CM-02 scheme. While this reduction successfully corrects the previous mass overestimation, it simultaneously weakens the spatial signal of the quartz plume. As the absolute mass loading in the coarsest bins approaches more realistic, the correlation coefficient becomes increasingly sensitive to localized transport mismatches and the potential 'wash-out' of coarse particles before they reach distant observational sites.

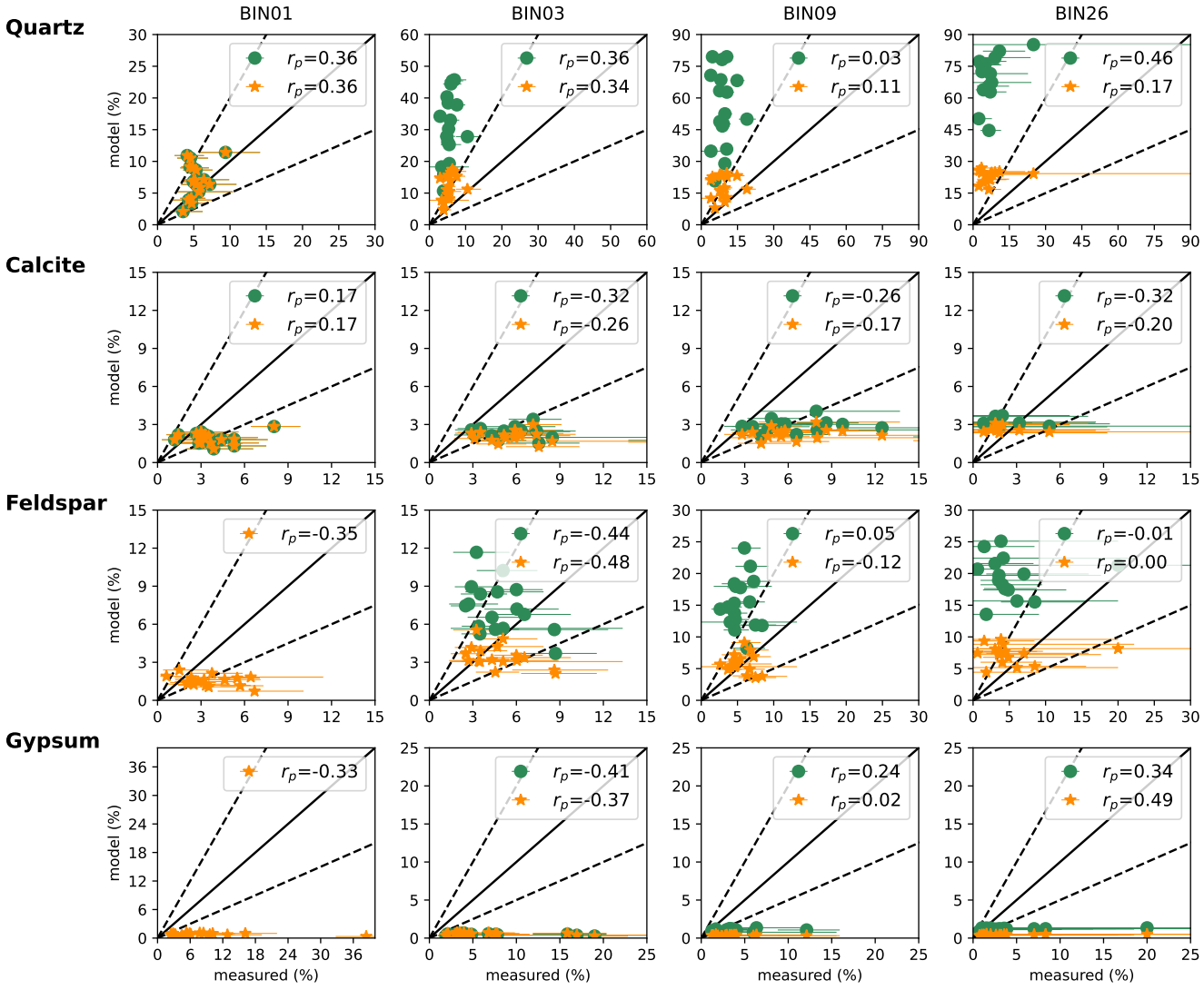

Figure 7. As in Fig. 6 but for quartz, calcite, feldspar, and gypsum. Note: Axis scales vary between panels to optimize the visibility of the fine fractions for quartz, feldspar and gypsum

Similarly, feldspar shifts from strong overestimation in JAT-CM-01, particularly in the coarser size bins, significantly less biased results across sizes (±1–2%) in JAT-CM-02 (Table 5). Interestingly, this localized success during the JATAC 2022 contrasts with the broader North African compilation, where the mass reduction exacerbated existing discrepancies (Table 4). Furthermore, these quantitative improvements in mass magnitude are not reflected in the spatial correlations, which show no improvement across any of the size ranges.

In contrast, calcite and gypsum remain consistently underestimated across all size fractions, with these tendencies generally worsening under the JAT-CM-02 scheme. For calcite, these results align with previous findings for 2–20 µm particles (Gonçalves Ageitos et al., 2023) and the broader North African measurement compilation comparison (Fig. 5). Correlation coefficients for calcite either remain stable or improve marginally under JAT-CM-02, yet they remain negative. Gypsum underestimation is further exacerbated in JAT-CM-02; notably, the r_{p} for BIN09 degrades despite moderate agreement for BIN26, where JAT-CM-02 shows a meaningful improvement.

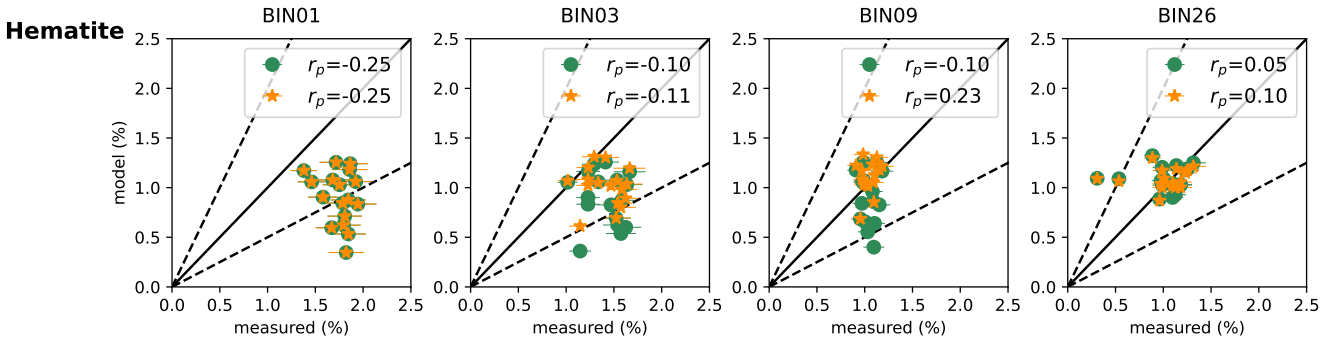

Figure 8. As in Figs.(6 & 7) but for hematite by following Eq. 23 replacing $w_{\mathrm{Feox\%}}$ by $w_{\mathrm{Hem\%}}$. Error bars represent 10% variation from the measurement.

Hematite (Fig. 8) is underestimated by an average of 0.9% in BIN01 under both modeling schemes, with mean biases decreasing in the larger size fractions. In BIN03, the JAT-CM-02 run slightly reduces the bias, while in BIN09 and BIN26, the two schemes diverge minimally, both yielding near-zero mean biases (0.1%). On average, hematite mass increases modestly by 5% in the 'modified' scheme. While r_{p} values remain similar in the finer size fractions, the JAT-CM-02 framework shows a notable, albeit weak, improvement for the coarser bins (e.g., BIN09). This is the first instance in which the 'modified' scheme demonstrates a clear advancement in the spatial representation of hematite. Despite persistent biases, hematite (Fig. 8) shows encouraging agreement with observations, supporting the scheme's robustness for applications sensitive to dust optical properties (e.g., Gómez Maqueo Anaya et al., 2025).

Averaged over the JATAC 2022 simulation period, the JAT-CM-02 produces substantial increases in phyllosilicates, illite, kaolinite, smectite, exhibiting 130% more mass relative to JAT-CM-01, alongside modest changes in hematite (+5%). Conversely, quartz (–61%), feldspar (–56%), and calcite (–14%), and gypsum (–17%) mass loadings decline significantly.

Collectively, these results suggest that while mass redistribution effectively addresses systematic magnitude biases for quartz and feldspar in this specific dataset, the underlying soil mineralogy maps remain a primary source of uncertainty. The persistent underrepresentation of calcite and gypsum, which seems to be independent of atmospheric model or dust emission parametrization (e.g., Gonçalves Ageitos et al., 2023), indicates that spatial correlation is limited more by source-map uncertainties than by the emission scheme itself.

5.2 Elemental composition

Cape Verde serves as a critical receptor site for Saharan dust, making its observational record uniquely suited for evaluating the 'modified' mineralogical scheme. In this section, we supplement our mineral-specific analysis with a validation of elemental mass fractions. By converting simulated mineral compositions into elemental abundances (via the relationships defined in Table 3), we establish a secondary, independent metric for assessing model performance.

While size-resolved elemental comparisons provide a broader perspective on dust composition, they also introduce complexities inherent to field data. Neither modeling approach fully accounts for the observed elemental variability, as measured compositions frequently include non-dust constituents or minerals not simulated in the current framework.

This is particularly evident in the DUSTRISK 2022 dataset; because these measurements were conducted near the surface during the NH winter, they are more susceptible to interference from local emissions and/or biomass burning plumes from the Sahel (Tesche et al., 2011). In contrast, the JATAC 2022 observations were performed within Saharan Air Layer, typically considered as pure dust during NH summer. However, minor contamination during atmospheric transit remains possible.

5.2.1 JATAC 2022

Figure 9 compares the observed and simulated concentrations of Si, Al, Fe, and Ca. For silicon (Si), the differences between the two schemes are negligible in the finest fraction (BIN01; Table 6). However, in the intermediate size ranges (BIN03 and BIN09), the 'modified' scheme (JAT-CM-02) shifts the model from an overestimation to an underestimation. Notably, the magnitude of this underestimation exceeds the previous overestimation, result that initially seems to contradict the substantial quartz overestimation identified for these size categories (Table 5).

Since quartz is not the only contributor to Si mass (Table 3), this underestimation likely stems from the compounded effect of stark reductions in feldspar and quartz that are not fully compensated for by the increase in phyllosilicates. This supports a hypothesis that non-simulated, high-Si minerals, such as those in the mica (e.g., muscovite) or chlorite groups, may be missing from the model (Scheuvens et al., 2013), while adding to the measured Si mass. In the coarsest bin (BIN26), while both schemes overestimate Si, JAT-CM-02 significantly mitigates this bias, reducing the mean bias from 14.1% to 0.9% (Table 6). This improvement is directly attributable to the substantial reduction of quartz content in JAT-CM-02 for this size category (Table 5). Ultimately, this demonstrates that refining mineral abundances can effectively improve elemental mass representation even when spatial correlations remain stagnant or degrade, a trend consistent with quartz comparisons across both the North African compilation (Fig. 5) and the JATAC 2022 dataset (Fig. 7).

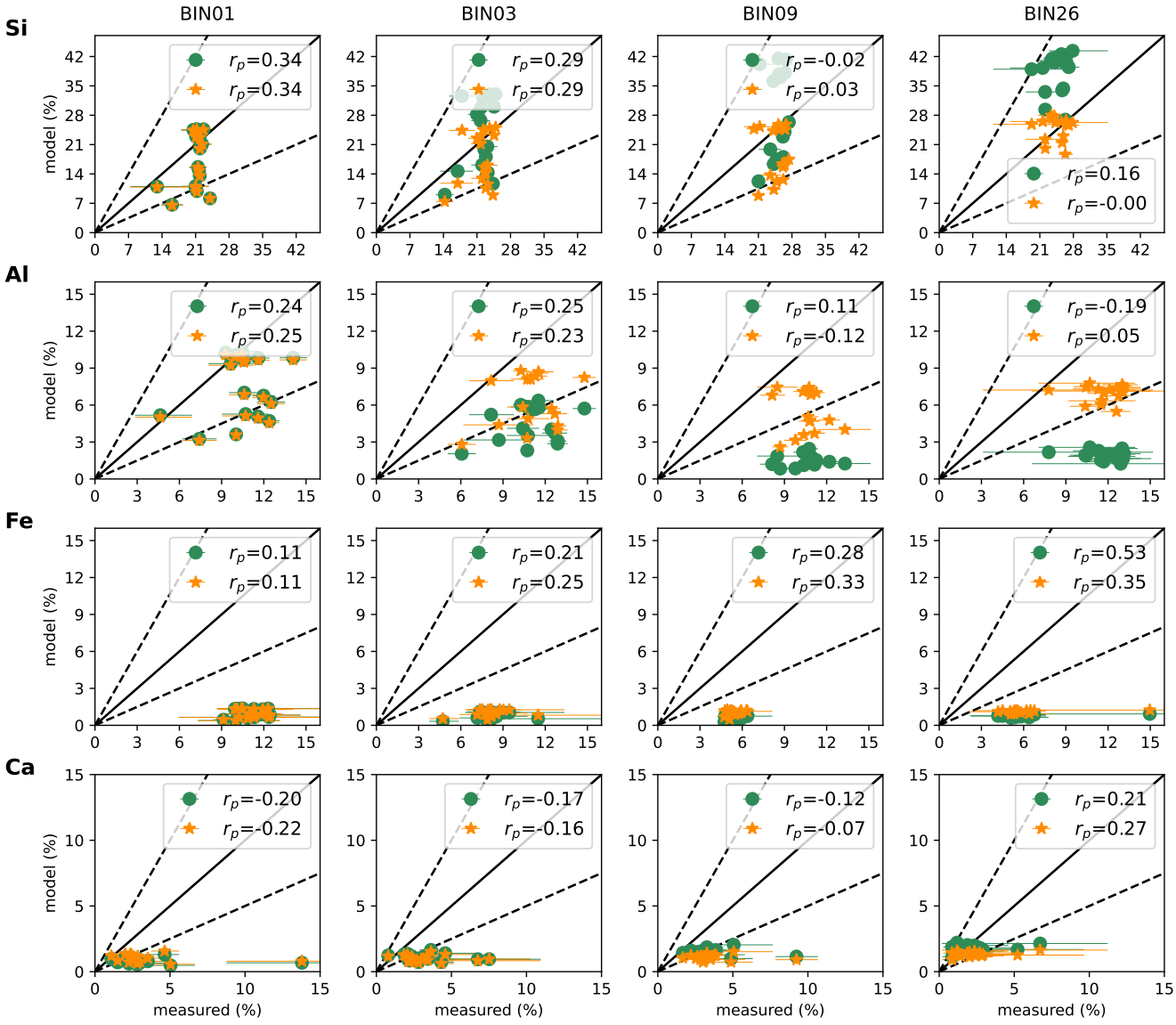

Figure 9. Scatterplots of observed elemental mass percentages of Si, Al, Fe, and Ca against simulated by COSMO5.05-MUSCAT. Simulated values were derived by multiplying modeled mineral mass by their respective elemental compositions (detailed in Table 3). Green solid circles indicate the 'original' mineral emission scheme (JAT-CM-01), while yellow solid stars represent the 'modified' version (JAT-CM-02). The titles of the columns are size classifications from COSMO5.05-MUSCAT (Table 1). The dashed lines represent the ratios of 2:1 and 1:2 between the simulated and observed mineral percentages. The error bars represent the lower and upper limits of the confidence intervals (between 2.5% and 97.5%).

Table 6. Mean bias (MB) of the elemental mass fractions for the 'original' (JAT-CM-01) and 'modified' (JAT-CM-02) schemes. The MB is calculated against the JATAC 2022 elemental measurements. The number of observation points used for each comparison is indicated in the parentheses (n).

Element	MB [%] (n)							
	JAT-CM-01				JAT-CM-02			
	BIN01	BIN03	BIN09	BIN26	BIN01	BIN03	BIN09	BIN26
Si	-3.6 (17)	0.4 (17)	4.4 (17)	14.1 (17)	-3.7 (17)	-4.5 (17)	-5.3 (17)	0.9 (17)
Al	-2.8 (17)	-6.5 (17)	-8.8 (17)	-9.4 (17)	-2.9 (17)	-4.6 (17)	-5 (17)	-4.4 (17)
Fe	-10.3 (17)	-7.6 (17)	-6 (17)	-5.2 (17)	-10.3 (17)	-7.4 (17)	-5.5 (17)	-4.8 (17)
Ca	-2.8 (17)	-2.3 (17)	-2.3 (17)	-1.2(17)	-2.6 (17)	-2.4 (17)	-2.7 (17)	-1.7 (17)
K	-0.2 (17)	-0.4 (17)	0.1 (17)	0.1 (17)	-0.1 (17)	-0.3 (17)	-0.1 (17)	-0.1 (17)
Mg	-1.2 (17)	-1.6 (17)	–	–	-1.2 (17)	-1.5 (17)	-1.5 (17)	-1.3 (17)
S	–	-1.1 (17)	-0.4 (17)	-0.4 (17)	-1.3 (17)	-1.1 (17)	-0.5 (17)	-0.5 (17)

Aluminum exhibits a clear size-dependent improvement across the bin-resolved mean biases (Table 6). While no significant changes occur in BIN01, all other size bins show a progressive reduction in underestimation. This improvement directly reflects the redistribution of clay minerals into larger size fractions within the 'modified' scheme, a shift that better captures the aggregated state of phyllosilicates during emission and atmospheric transport. Persistent underestimation, however, may be attributed to the presence of high-Al, non-simulated minerals such as chlorite (Scheuvens et al., 2013). This mass redistribution is particularly encouraging, as the resulting Al concentrations align more closely with observations than the individual mineral comparisons might suggest (Table 5). Nonetheless, these improvements in mass bias do not extend to the spatial correlation coefficients (r_{p}), which show a slight degradation in the JAT-CM-02 scheme (Fig. 9). This suggests that while the mass balance is improved, the inherently weak correlation, likely driven by the influence of non-simulated minerals, is further exacerbated by the proposed mass redistribution.

Iron (Fe) content shows negligible sensitivity to the choice of emission scheme choice across all size bins, as evidence by the persistent and severe underestimation exhibited by the mean bias for both approaches (Table 6). From JAT-CM-02 results, spatial correlations increase for BIN03 and BIN09 but deteriorate further for BIN26 (Fig. 9). Notably, the mineral-specific hematite comparison (Figs. 8 & 5) does not show a comparable underestimation, and while not all Fe is found in hematite, it is still a major carrier from which this level of discrepancy is unexpected. Therefore this discrepancy exposes a critical difference between mineralogical and elemental validation metrics. Given iron oxide's pivotal role in dust-atmosphere interactions (Li et al., 2024, 2021; Song et al., 2024; Zhang et al., 2024), this distinction carries significant implications for radiative and bio-geochemical modeling. This inconsistency reveals an inherent limitation of modeling frameworks that treat minerals as discrete particles with uniform composition.

The calcium (Ca) comparison in Fig. 9 reveals an increased underestimation in the JAT-CM-02 scheme across all size fractions. This result is consistent with the JATAC 2022 mineralogical analysis, where both schemes significantly underestimate the concentrations of calcite and gypsum, the primary Ca-bearing minerals currently simulated (Fig. 7). This bias is further exacerbated by the exclusion of dolomite, a major Ca-rich mineral (Formenti et al., 2014), not accounted for in the model simulations. Interestingly, while the spatial correlation increases for the coarsest fraction (BIN26), this may be an artifact of the sampling distribution; the remaining size bins show low or even negative correlations, with no discernible trend of improvement under the 'modified' scheme.

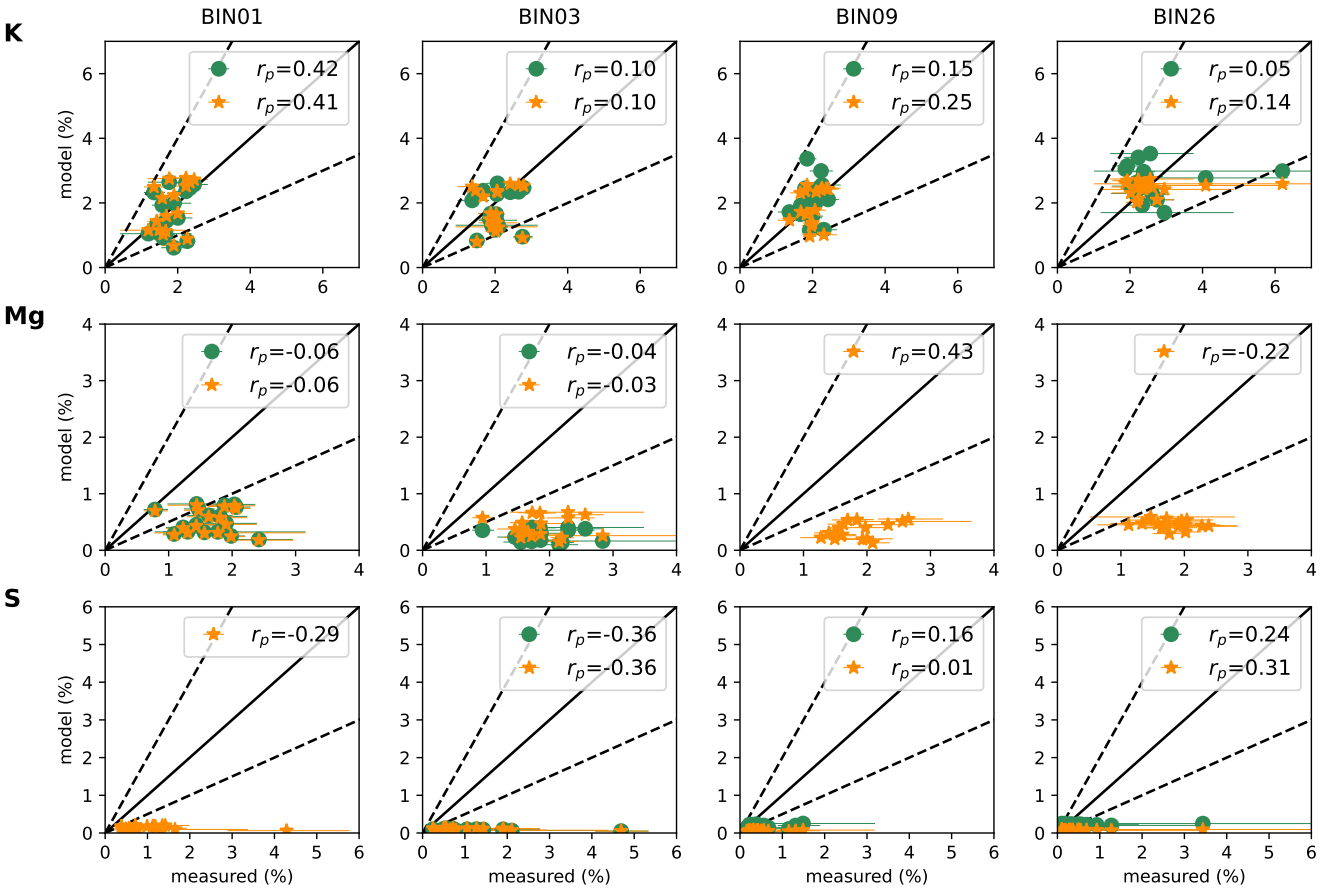

Figure 10. As in Fig. 9 but for K, Mg, and S.

Figure 10 presents the scatterplots comparing the simulated and measured content of K, Mg, and S. In the bin-resolved analysis for potassium (K), 'modified' scheme (JAT-CM-02) shows an improvement in both BIN01 and BIN03, resulting in lower mean biases. In contrast, BIN09 and BIN26 transition from an overestimation in JAT-CM-01 to an underestimation of comparable magnitude in JAT-CM-02 (Table 6).

Interestingly, while the mineral-specific feldspar comparison (Fig. 7) also showed a uniform improvement across all sizes for JAT-CM-02, the reduction in bias between schemes was more striking for feldspar than for elemental K. This suggests that potassium partitioning is influenced by factors beyond feldspar size distribution alone; specifically, both illite and feldspar contribute to the K budget, alongside non-simulated minerals such as white mica. Nevertheless, the mean biases indicate a reasonable agreement between simulated and observed K mass. The increase in r_{p} values for the two largest size categories in JAT-CM-02 is encouraging, suggesting that the explicit inclusion of illite in these fractions provides a more representative spatial and mass distribution. This stands in contrast to the spatial correlation coefficients for feldspar and illite, which oscillate between weak and negative, (Fig. 7). These discrepancies highlight the value of elemental-level validation in assessing modifications to mineralogical emission schemes, as changes that appear modest in mineral-specific comparisons may produce clearer signals when evaluated through their elemental signatures.

Both emission schemes underestimate magnesium (Mg) in the size-resolved analysis, with no significant differences between the measured mean bias for JAT-CM-01 and JAT-CM-02 (Table 6). This persistent underestimation mirrors the the results for illite, the sole Mg-bearing mineral currently simulated, which exhibits a dramatic underrepresentation by the model (Fig. 6). Interestingly, while the underestimation for illite intensifies in coarser size categories, this trend is not observed for Mg. This divergence suggests two possibilities: either the illite is being misclassified, a common hurdle in complex mineralogical assemblages (e.g., Rieder et al., 1998), or the Mg content assigned to illite in Table 3 is insufficient. Notably, the moderate r_{p} values found for BIN09 supports the conclusion that the inclusion of illite in larger size fractions is a more physically representative approach to simulating this mineral's distribution. However, the low correlation values in the remaining bins likely reflect the absence of additional Mg sources in the model such as the high-Mg mineral dolomite (Formenti et al., 2014).

Sulfur is consistently and substantially underestimated by the model across both emission schemes in the bin-resolved comparison (Fig. 10 and Table 6). This deficiency directly reflects the earlier gypsum-specific mineral comparison (Fig. 7 and Table 5) and is attributable to the well-documented underrepresentation of gypsum content in SMAs (Gonçalves Ageitos et al., 2023).

Overall, the transition to the 'modified' scheme demonstrates that refining mineralogical size distributions, specifically the aggregation of phyllosilicates and the reduction of coarse-mode quartz, significantly improves the model's ability to replicate observed elemental mass balances for Si, Al, and K. However, these improvements are not uniformly reflected in the spatial correlation coefficients (r_{p}), which remain sensitive to the inherent limitations of the current modeling framework.

A notable discrepancy persists for iron; while simulated hematite shows reasonable agreement with observations, total elemental Fe remains severely underestimated across both schemes. This inconsistency underscores a critical disconnect between discrete mineral modeling and the chemical complexity of natural dust. These discrepancies point to a compounded effect of missing mineral phases (e.g., dolomite, muscovite, and chlorite) and the presence of "hidden" elements within nanoscale oxide coatings and silicate aggregates (Kandler et al., 2009; Lafon et al., 2004; Scheuvens et al., 2013). Consequently, while the mass redistribution in JAT-CM-02 moves toward a more physically representative simulation of dust chemistry, a complete elemental closure will likely require the inclusion of these non-simulated minerals and, for Fe, a shift away from assuming uniform mineral compositions across all size fractions.

Table 7. Mean bias (MB) of the elemental mass fractions for the 'original' (DUST-CM-01) and 'modified' (DUST-CM-02) schemes. The MB is calculated against the DUSTRISK 2022 elemental measurements. The number of observation points used for each comparison is indicated in the parentheses (n).

Element	MB [%] (n)			
	DUST-CM-01		DUST-CM-02	
	PM2.5	PM10	PM2.5	PM10
Al	6.6 (34)	-4.6 (45)	4.7 (34)	-1.2 (45)
Fe	-2 (34)	-1.7 (45)	-2.1 (34)	-1.4 (45)
Ca	-2.2 (34)	-4.8 (45)	-2.3 (34)	-4.8 (45)
K	2.3 (34)	0.9 (45)	1 (34)	1.1 (45)
Mg	0.1 (33)	-0.6 (40)	-0.1 (33)	-0.3 (40)
S	-0.7 (34)	-0.8 (45)	-0.7 (34)	-0.8 (45)

5.2.2 DUSTRISK 2022 campaign

The scatterplots in Fig. 11 demonstrate marked differences in performance between the 'original' (DUST-CM-01) and 'modified' (DUST-CM-02) mineral emission schemes when evaluated across elemental composition and particle size categories (mean biases detailed in Table 7).

The DUST-CM-02 approach shows a better representation for aluminum, resulting in higher concentrations and greater variability in PM10 compared to PM2.5. For the PM2.5, the modest reduction in phyllosilicate mass under DUST-CM-02 mitigates model overestimation, with mean biases improving from 6.6% to 4.7%. Conversely, increased phyllosilicate concentrations in the PM10 fraction, reduces the previous underestimation from -4.6% to -1.2% (Table 7). While these improvements in the coarse fraction align with the JATAC 2022 elemental comparison (Fig. 9), the PM2.5 overestimation persists in the DUSTRISK 2022 samples but not in JATAC 2022. This discrepancy might be due to methodological differences in fine particle measurement between campaigns. Notably, DUST-CM-02 shows improved spatial correlations for the fine fraction, but not for the coarser fraction (Fig. 11), mirroring the JATAC 2022 comparison results (Fig. 9). This divergence and the consistent underestimation of aluminum in coarser sizes suggests that the model may be missing a specific Al-rich coarse mineral phase, such as muscovite (Scheuvens et al., 2013).

Both emission schemes substantially underestimate iron content, with DUST-CM-02 offering negligible improvement. This systematic underestimation, consistent with the JATAC 2022 elemental comparison (Fig. 9 & Table 6), stands in contrast with the mineral-level evaluation, where simulated hematite concentrations align comparatively better with observations (Figs. 5 & 8). While Fe is present in some forms of smectite, our current framework uses montmorillonite as the proxy for the smectite group due to its dominance in Saharan dust pathways toward Cape Verde (Moreno et al., 2006). Substituting montmorillonite with an Fe-rich smectite like nontronite would contribute approximately 22% of the smectite mass to the iron budget; however, this

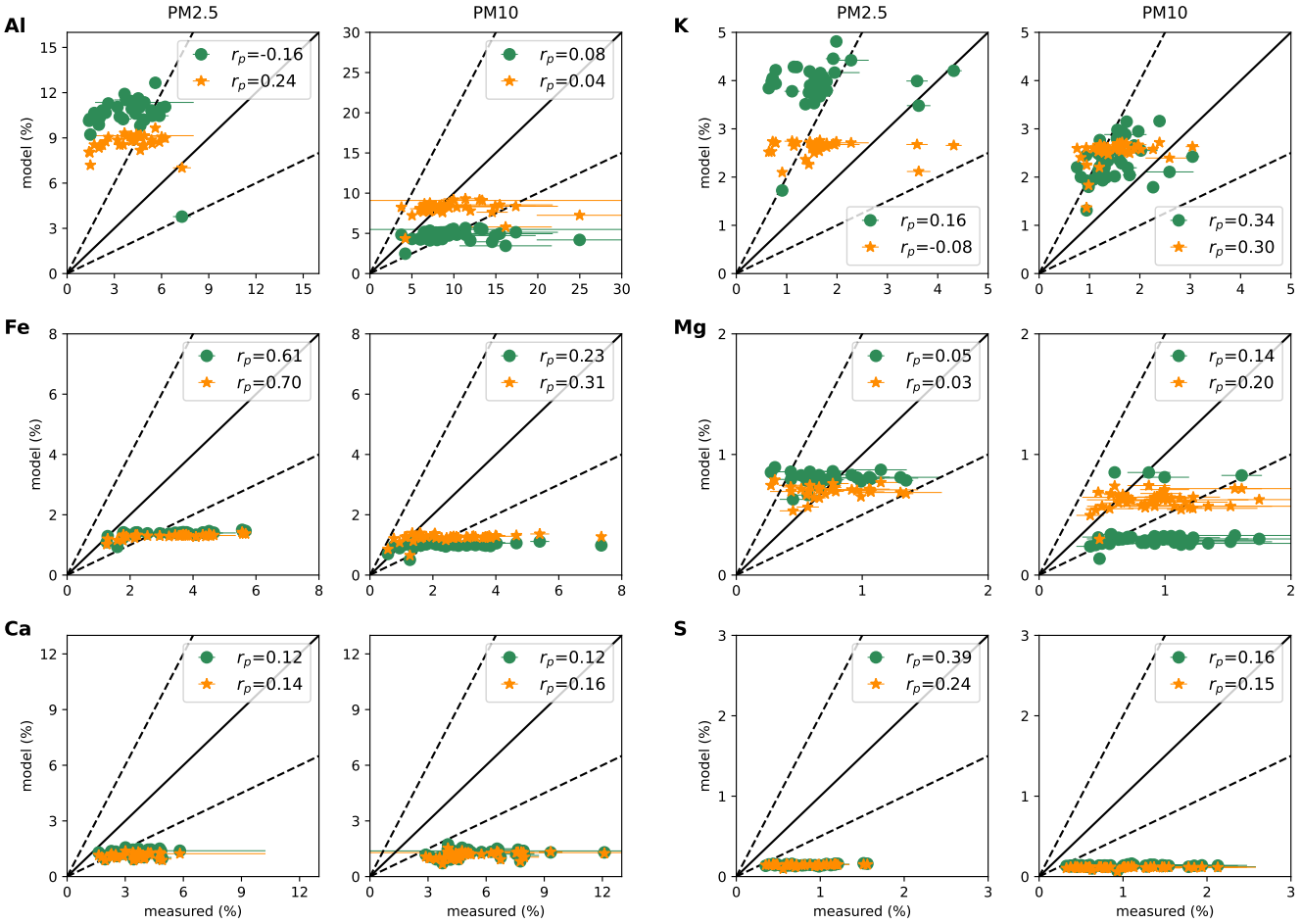

Figure 11. Scatterplots comparing observed elemental mass percentages of Al, Fe, Ca, K, Mg, and S against simulated values from COSMO5.05-MUSCAT. Simulated values were derived by multiplying modeled mineral mass by their respective elemental compositions (detailed in Table 3). Green solid circles indicate the 'original' mineral emission scheme (DUST-CM-01), while yellow solid stars represent the 'modified' version (DUST-CM-02). Column headers denote size classifications based on in-situ filter measurements: PM2.5 and PM10. The error bars represent the measurements' standard deviation. Dashed lines mark the 2:1 and 1:2 ratios between simulated and observed mineral percentages. Note: Axis scales vary between PM2.5 and PM10 panels for Al to optimize the visibility.

adjustment remains insufficient to bridge the substantial gap between the model and measurements (Tables 6 & 7). Regarding the spatial correlation coefficients, r_{p} for PM2.5 is the highest among all comparisons and further improves with DUST-CM-02. Conversely, correlations for the PM10 are only moderate, though they also show improvement with DUST-CM-02. Interestingly, the model exhibits an inverse relationship between size fraction and correlation strength, with the finest particles yielding the most robust spatial agreement, and simultaneously exhibit a worse mean bias (Fig. 11 & Table 7).

Calcium shows a consistent systematic underestimation across both schemes (Table 7), directly mirroring the underrepresentation of calcite and gypsum (Figs. 5 & 7). While DUST-CM-02 provides a marginal improvement in r_{p}, the correlation coefficients for both size categories remain notably similar (Fig. 11). This consistency between size fractions stands in contrast to the JATAC 2022 results (Fig. 9), where positive, albeit weak, correlations were restricted exclusively to the coarsest size category.

The potassium content illustrated in Figure 11 reveals an intriguing, size-specific improvement under the DUST-CM-02 scheme. For the PM2.5 fraction, the modified approach yields better agreement with observations, reducing the mean bias from 2.3% to 1%, while PM10 remains largely unchanged (Table 7). This bias reduction stems primarily from the reallocation of feldspar fractions into the finer size category. Such an improvement is particularly noteworthy because the preceding mineral evaluation of feldspar (Figs. 5 & 7) showed inconsistent performance. These results partially mirror the JATAC 2022 elemental comparison (Fig. 10), where potassium showed the most significant improvements. However, the discrepancies between campaigns, such as the PM2.5 overestimation which contrasts with JATAC 2022 results (Table 6), likely reflect seasonal shift in active dust source regions between the NH winter and summer (Schepanski et al., 2009).

For the fine potassium fraction specifically, the consistently low r_{p} values in both schemes suggest that the simulated spatial distribution does not align with observations. This decoupling points toward an additional, non-simulated K source; given that the observations coincide with the NH winter, this discrepancy could be attributable to Sahelian biomass burning (Tesche et al., 2011), a well-documented regional contributor of fine-mode potassium (Dang et al., 2022; Jahn et al., 2021). Although the current model overestimation in both DUST-CM-01 and DUST-CM-02 (Table 7) would superficially argue against the need for additional K mass, the poor spatial correlation suggests that the total observed K is governed by a combination of dust and possible biomass burning patterns that the dust-only schemes cannot reconcile.

Magnesium displays a size-dependent performance pattern analogous to that of aluminum (Fig. 11). Although the earlier illite comparison showed a clear underestimation under the 'modified' scheme (Fig. 6), this Mg elemental analysis reveals a clear enhancement in model representation. In the PM2.5 fraction, DUST-CM-02 shifts the model from a slight overestimation to a slight underestimation, while for PM10, the underestimation is significantly reduced, with mean biases effectively halved (Table 7). In comparison, the JATAC 2022 dataset exhibits a more severe Mg underestimation, highlighting the variability across campaigns. Despite these differences in magnitude, both datasets demonstrate consistent size-dependent improvements and strengthened correlation coefficients under the 'modified' scheme, particularly within the PM10 and BIN09 size categories (Figs. 11 & 10). This cross-campaign consistency reinforces the conclusion that the redistribution of minerals into coarser fractions, specifically Mg-bearing illite, yields a more robust representation of the dust plume's mineralogy.

In contrast, sulfur remains systematically and substantially underestimated across both emission schemes. This persistent bias is accompanied by a deterioration in r_p values (Fig. 11 & Table 7) mirroring the poor performance observed in the JATAC 2022 dataset (Fig. 10).

The elemental comparisons reveal that while the 'modified' emission scheme successfully addresses several key biases on the mineralogical representation, particularly for Si, Al, and Mg, systematic underestimations persist for certain elements, notably Fe, Ca, and S. Interpretation of these discrepancies must consider potential contributions from non-mineral sources, given that the sampling campaign employed long integration periods during the NH winter, a season characterized by intense Sahelian biomass burning activity (Tesche et al., 2011). While biomass burning emissions typically contribute K, Mg, Fe, and Al to the fine aerosol fraction (Dang et al., 2022; Jahn et al., 2021; Paris et al., 2010), the model continues to overestimate Al and K content despite the improvements in DUST-CM-02. Furthermore, the high accuracy of the Mg simulation suggests that biomass burning may not be the primary driver of the observed mass concentrations in these samples. However, while a minor fraction of the missing Fe could be attributed to biomass burning, the persistence of this underestimation across multiple campaigns (Tables 7 & 6) points more definitively toward a fundamental modeling oversight by omitting Fe-rich minerals and by the simplified assumption of external mineral mixing (discrete particles).

Together, these results highlight both the progress achieved with the 'modified' scheme and the persistent challenges facing mineral dust modeling frameworks. The improved representation of quartz and feldspar demonstrates that refined emission PSDs and mineral abundances can effectively propagate through the model to enhance both mineralogical and elemental fidelity. However, persistent discrepancies in elemental composition, compounded with campaign-specific variability, underscore fundamental structural limitations. Specifically, current frameworks struggle to represent the heterogeneous internal mixing of iron oxides and the complex speciation of magnesium within silicate aggregates. Furthermore, omissions within the soil mineralogy database remain a significant bottleneck. Addressing these limitations will require not only continued refinement of soil mineral assemblage databases and emission parameterizations, but also expanded observational constraints spanning multiple seasons, source regions, and atmospheric conditions to capture the full complexity of mineral dust composition.

6 Conclusions

The implementation of the 'modified' mineral simulation approach in COSMO5.05-MUSCAT significantly enhances the representation of dust aerosol composition, as demonstrated by the DUST-CM-02 and JAT-CM-02 simulation periods. By adjusting the soil mineralogical database PSD prior to emission flux calculations, the model provides a substantially more accurate depiction of phyllosilicates and quartz when compared against North African aerosol measurements (Fig. 5). It effectively resolves the systematic quartz overestimation (Table 4), which validates the redistribution logic. The persistent underestimation of calcite and weak hematite correlations suggest that aerodynamic repartitioning alone cannot compensate for fundamental uncertainties in source soil mineralogy.

Validation with in-situ elemental concentration-based, mineral phases measurements from JATAC 2022 further confirmed these improvements (Figs. 6 & 7). Validation across discrete size bins confirms that the 'modified' scheme successfully extends

the model's predictive skill into a broader size spectrum, particularly for silicon- and potassium-bearing minerals. However, the occasional decoupling of improved mean bias from stable or weakened spatial correlations indicates that while the total mass balance is now more realistic, the model's sensitivity to specific source-region variability remains a challenge that purely structural scheme changes cannot yet overcome.

The complementary elemental validation for DUSTRISK and JATAC 2022 campaigns highlights both the strengths and the inherent limitations of current modeling frameworks. Across both campaigns, elemental concentrations largely mirrored their mineralogical counterparts. Specifically the correction of silicon and potassium biases demonstrates the consistency and improvement of the 'modified' scheme. The successful refinement of aluminum concentrations across all size fractions further confirms that a more representative size-dependent distribution of phyllosilicates is key to bridging the gap between simulated mineralogy and in-situ observations (Figs. 10 & 11 and Tables 6 & 7).

While the model achieved a more representative size-dependent distribution of phyllosilicates, important discrepancies remain regarding spatial correlation. The differentiated spatial correlations suggest that model benefits are primarily concentrated in the finer size ranges; the persistent mismatch in coarser fractions likely stems from the omission of specific Al-rich coarse minerals, such as muscovite (Scheuvens et al., 2013).

This mineralogical gap is further reflected by the magnesium results. Across both the JATAC and DUSTRISK 2022 datasets, the underestimation of Mg is notably less severe than the pronounced underrepresentation of illite. Given that illite is the sole Mg-bearing mineral in the current model configuration, this discrepancy suggests that the elemental Mg budget is influenced by factors beyond the simulated illite mass alone. This relative "success" in Mg representation compared to the illite mass bias could be due to natural Saharan illite posing a higher degree of Mg-substitution than is currently assumed in the model's static stoichiometry. The persistence of these biases indicates that current soil mineral assemblages fail to accurately capture Mg speciation within mixed silicate aggregates (Kandler et al., 2018). Collectively, these findings underscore that future improvements in model fidelity will require a more comprehensive and complex mineralogical inventory that spans the full particle size spectrum.

Furthermore, significant inter-campaign discrepancies reveal that model validation is inherently sensitive to external factors beyond emission parameterization. For instance, the shift from aluminum underestimation in JATAC 2022 to overestimation in the finest fraction of DUSTRISK 2022 suggests underlying methodological differences in campaign sampling. Furthermore, the more severe Mg deficit noted in JATAC 2022 could reflect reduced biomass burning interference during the NH summer SAL sampling rather than a shift in model performance (Figs. 10 & 11).

The persistent underestimation of elemental iron (Figs. 9 & 11), despite adequate hematite mass fractions (Figs. 5 & 8), highlights a fundamental limitation in treating minerals as internally homogeneous. This mineral-element discrepancy exposes a critical modeling limitation: iron exists predominantly as nanoscale oxide coatings or inclusions within other mineral phases (Lafon et al., 2004; Kandler et al., 2007) rather than as discrete particles. This structural complexity is intrinsically difficult to capture for frameworks that treat minerals as internally homogeneous particles. However, the high correlation coefficients observed for the DUSTRISK 2022 finest fractions indicate that while the total mass is shifted, the model effectively simulates the transport dynamics of iron-bearing clays. Beyond structural complexities, the observed underestimation may also stem from

the selection of a non-iron-bearing smectite for this analysis, as well as the exclusion of other iron-contributing minerals from the model.

The persistent underestimation of calcite and gypsum further underscores the limitations of traditional, dispersive soil analysis methods, such as wet-sieving, for constraining dust emission schemes. These methodologies likely dissolve or redistribute soluble minerals as these two, failing to represent the natural state of soil aggregates. Given that shifting initial soil assumptions can alter mineral mass fractions by over 130%, the high sensitivity of the model demonstrates that achieving mineralogical fidelity requires a transition toward non-dispersive soil sampling techniques that preserve the physical and chemical integrity of the parent soil.

The seasonal comparison between DUSTRISK (NH winter) and JATAC (NH summer) 2022 further underlines the influence of source region activity. While phyllosilicate increases were consistent across seasons, calcite decreased more strongly during summer (–14%), together with further declines in quartz, feldspar, and gypsum content. These differences reflect shifts in dominant dust-emitting regions and associated meteorology, underscoring the need to account for temporal variability when evaluating mineral fractions in transport models.

Taken together, these results demonstrate both progress and remaining challenges in modeling dust mineralogy. The 'modified' scheme clearly improves the size-resolved representation of phyllosilicates, quartz, and feldspar across both mineral and elemental scales. However, persistent biases in iron, calcium, and magnesium highlight the inherent limitations in representing the heterogeneous internal mixing and complex speciation of natural mineral dust. Critically, the elemental validation approach employed here provides a complementary and previously underutilized pathway for model evaluation. By converting simulated mineral compositions to elemental mass fractions and comparing them against measured elemental abundances, this methodology offers several distinct advantages. First, it enables validation against the extensive body of published elemental composition measurements from techniques such as X-ray fluorescence and electron microscopy. Second, it exposes discrepancies between mineral-level and element-level performance that would remain hidden in mineral-only comparisons. Third, it provides independent constraints on mineralogical simulations that can reveal limitations in both emission parameterizations and fundamental assumptions about particle internal structure. The mineral-element discrepancies identified for Fe exemplify how this dual validation framework diagnoses complexities in dust composition that direct mineral measurements alone cannot adequately capture, underscoring its value for advancing mineralogical representation in atmospheric models.

Future progress will depend on improved mineralogical datasets, better integration of observations into models, and advances in representing the internal complexity of mineral dust particles. The emergence of hyperspectral measurements from NASA's EMIT mission (Green et al., 2020), alongside field campaigns providing detailed size-resolved composition at both mineral and elemental levels, offers a pathway to reduce current uncertainties. Incorporating such multi-scale observations, particularly for iron oxides and mixed silicate phases, will help resolve biases in key radiatively active minerals and improve constraints on dust–climate interactions. Additionally, developing modeling frameworks that can represent minerals as internally mixed aggregates rather than discrete particles may be necessary to bridge the persistent mineral-element discrepancies identified here. Recent studies (Li et al., 2021, 2024; Obiso et al., 2024) reinforce that refining soil mineral maps and dust size distributions is critical for advancing our understanding of dust's climatic and biogeochemical roles.

Table A1. Ideal normalized mass compositions for the modeled mineral classes. Elements not shown are zero. Value ranges are derived from data by Journet et al. (2008) and https://webmineral.com/.

Class name	Atomic range	Value range
Kaolinite	Si	0.486
	Al	0.483
	Fe	0.01
	Ti	0.02
Illite	Mg	0.027
	K	0.09
	Al	0.218
	Si	0.538
	Ca	0.03
	Fe	0.07
	Ti	0.01
Smectite	Mg	0.029
	Al	0.211
	Si	0.673
	Ca	0.022
	Fe	0.06

Class name	Atomic range	Value range
Quartz	Si	1.0
Calcite	Ca	1.0
Gypsum	Ca	0.554
	S	0.445
Feldspar	Na	0.02
	Al	0.238
	Si	0.538
	K	0.1
	Ca	0.08
	Fe	0.01
Hematite	Fe	0.9
	Si	0.04
	Al	0.06

Data availability. The dataset for reproducing the graphs presented here are available at https://doi.org/10.5281/zenodo.19731364

.

A JATAC in-situ aerosol measurements: mineral phase criteria

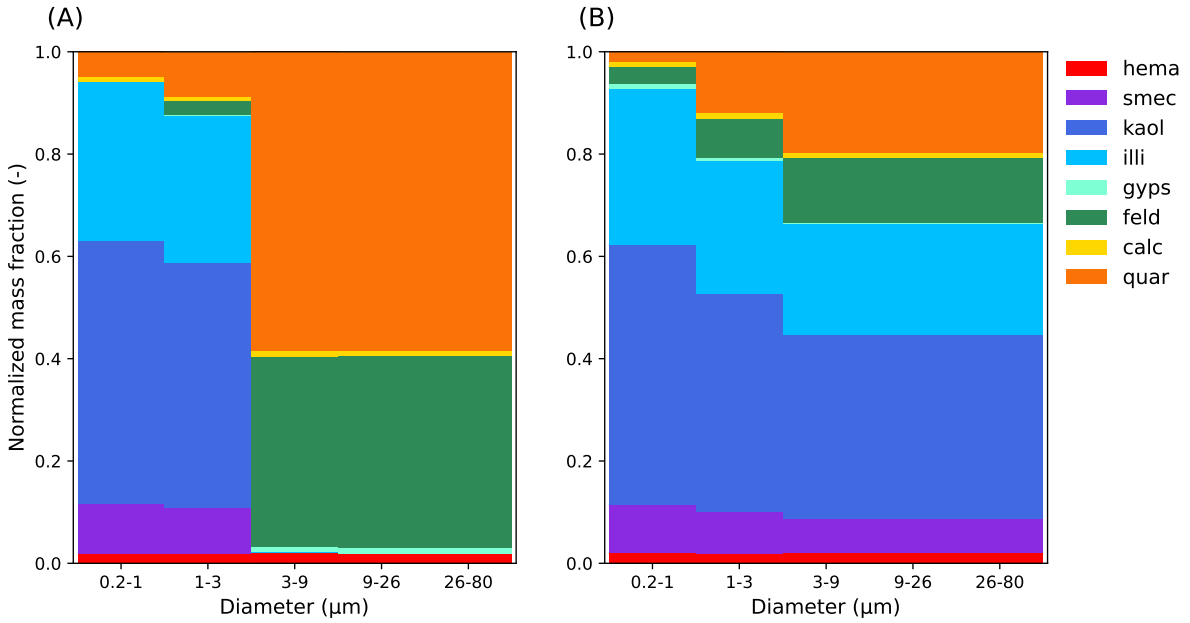

Figure B1. Comparison of normalized mineral mass size distributions for the Haplic Xerosol soil type located in the northwestern Sahara (22.75°N, 6.5°W). Panel (A) illustrates the soil mineral physical size distributions (PSDs) according to the GMINER database. Panel (B) depicts the resulting emitted aerosol mineral PSDs, representing the initial state of the dust plume immediately following emission. The aerosol PSD is derived by applying the BFT-based modification approach (Perlwitz et al., 2015a; Gonçalves Ageitos et al., 2023) to the underlying soil data. Quar: quartz; calc: calcite; feld: feldspars; gyps: gypsum; illi: illite; kaol: kaolinite; smec: smectite; hema: hematite.

B COSMO5.05-MUSCAT Haplic Xerosols

Author contributions. SGMA drafted the manuscript. SA, KK, DA, MK, MH, IT, and KS reviewed and edited the manuscript. SGMA, HB, DA, BH, MH, and KS contributed to the conceptualization of the study. SGMA prepared the figures and organized the datasets. EJSS and KWF were responsible for the elemental analysis of samples collected during the DUSTRISK 2022 campaign. SA and KK conducted the elemental analysis and mineral characterization of the samples collected by MK during the JATAC 2022 campaign. MF led the software development by restructuring the code associated with the MUSCAT dust emission scheme. SGMA, MF, BH, KS, and IT contributed to code development related to the inclusion of mineralogy. SGMA, SA, KK, and KS performed the formal data analysis.

Competing interests. The authors declare that they have no conflict of interest

Acknowledgements. This study is done in the framework of the DUSTRISK (a risk index for health effects of mineral dust and associated microbes) project, funded by the Leibniz Collaborative Excellence Programme Project (grant number K255/2019).

This research has been supported by the German Federal Ministry for Economic Affairs and Energy (BMWi) (grant no. 50EE1721C). Furthermore, we also acknowledge the support through ACTRIS-2 under grant agreement no. 654109 from the European Union's Horizon 2020 research and innovation programme and ACTRIS PPP under the Horizon 2020 – Research and Innovation Framework Programme, H2020-INFRADEV- 2016-2017, Grant Agreement number: 7395302.

We acknowledge and thank the team of OSCM / INMG for their crucial and ongoing support. We further thank ESA and the ASKOS/JATAC teams for the organization of the JATAC(s) campaign(s) and their continuous support.

Further thanks are due to the Deutscher Wetterdienst (DWD) for cooperation and support. We also gratefully acknowledge the Darmstadt Institute for their thorough analysis of the samples, for sharing the results, and for tailoring the analyses to the specific needs of this study. We further thank the National Observatory of Athens for collecting the samples.

Furthermore, ChatGPT and Gemini were utilized to rephrase and shorten sentences, as well to identify the appropriate prepositions.

References

Adedokun, J. A., Emofurieta, W. O., and Adedeji, O. A.: Physical, mineralogical and chemical properties of harmattan dust at Ile-Ife, Nigeria, Theoretical and Applied Climatology, 40, 161–169, https://doi.org/10.1007/BF00866179, 1989.

Alastuey, A., Querol, X., Castillo, S., Escudero, M., Avila, A., Cuevas, E., Torres, C., Romero, P.-M., Exposito, F., García, O., Pedro Diaz, J., Dingenen, R. V., and Putaud, J. P.: Characterisation of TSP and PM2.5 at Izaña and Sta. Cruz de Tenerife (Canary Islands, Spain) during a Saharan Dust Episode (July 2002), Atmospheric Environment, 39, 4715–4728, https://doi.org/10.1016/j.atmosenv.2005.04.018, 2005.

Albani, S., Mahowald, N. M., Perry, A. T., Scanza, R. A., Zender, C. S., Heavens, N. G., Maggi, V., Kok, J. F., and Otto-Bliesner, B. L.: Improved dust representation in the Community Atmosphere Model, Journal of Advances in Modeling Earth Systems, 6, 541–570, https://doi.org/10.1002/2013MS000279, 2014.

Aryasree, S., Kandler, K., Benker, N., Walser, A., Tipka, A., Dollner, M., Seibert, P., and Weinzierl, B.: Vertical Variability in morphology, chemistry and optical properties of the transported Saharan air layer measured from Cape Verde and the Caribbean, Royal Society Open Science, 11, 231 433, https://doi.org/10.1098/rsos.231433, 2024.

Baldauf, M., Seifert, A., Förstner, J., Majewski, D., Raschendorfer, M., and Reinhardt, T.: Operational Convective-Scale Numerical Weather Prediction with the COSMO Model: Description and Sensitivities, Monthly Weather Review, 139, 3887–3905, https://doi.org/10.1175/MWR-D-10-05013.1, 2011.

Balkanski, Y., Schulz, M., Claquin, T., and Guibert, S.: Reevaluation of Mineral aerosol radiative forcings suggests a better agreement with satellite and AERONET data, Atmospheric Chemistry and Physics, 7, 81–95, https://doi.org/10.5194/acp-7-81-2007, 2007.

Barkan, J., Kutiel, H., Alpert, P., and Kishcha, P.: Synoptics of dust intrusion days from the African continent into the Atlantic Ocean, Journal of Geophysical Research: Atmospheres, 109, 2003JD004 416, https://doi.org/10.1029/2003JD004416, 2004.

Berge, E.: Transboundary air pollution in Europe. Part 2: Numerical addendum to emissions, dispersion and trends of acidifying and eutrophying agents, https://www.osti.gov/etdeweb/biblio/646220, 1997.

Bredeck, G., Dos S. Souza, E. J., Wigmann, C., Fomba, K. W., Herrmann, H., and Schins, R. P.: The influence of long-range transported Saharan dust on the inflammatory potency of ambient PM2.5 and PM10, Environmental Research, 252, 119 008, https://doi.org/10.1016/j.envres.2024.119008, 2024.

Caquineau, S., Gaudichet, A., Gomes, L., Magonthier, M.-C., and Chatenet, B.: Saharan dust: Clay ratio as a relevant tracer to assess the origin of soil-derived aerosols, Geophysical Research Letters, 25, 983–986, https://doi.org/10.1029/98GL00569, 1998.

Cardoso, J., Almeida, S. M., Nunes, T., Almeida-Silva, M., Cerqueira, M., Alves, C., Rocha, F., Chaves, P., Reis, M., Salvador, P., Artiñano, B., and Pio, C.: Source apportionment of atmospheric aerosol in a marine dusty environment by ionic/composition mass balance (IMB), Atmospheric Chemistry and Physics, 18, 13 215–13 230, https://doi.org/10.5194/acp-18-13215-2018, 2018.

Chatziparaschos, M., Daskalakis, N., Myriokefalitakis, S., Kalivitis, N., Nenes, A., Gonçalves Ageitos, M., Costa-Surós, M., Pérez García-Pando, C., Zanoli, M., Vrekoussis, M., and Kanakidou, M.: Role of K-feldspar and quartz in global ice nucleation by mineral dust in mixed-phase clouds, Atmospheric Chemistry and Physics, 23, 1785–1801, https://doi.org/10.5194/acp-23-1785-2023, 2023.

Dang, C., Segal-Rozenhaimer, M., Che, H., Zhang, L., Formenti, P., Taylor, J., Dobracki, A., Purdue, S., Wong, P.-S., Nenes, A., Sedlacek III, A., Coe, H., Redemann, J., Zuidema, P., Howell, S., and Haywood, J.: Biomass burning and marine aerosol processing over the southeast Atlantic Ocean: a TEM single-particle analysis, Atmospheric Chemistry and Physics, 22, 9389–9412, https://doi.org/10.5194/acp-22-9389-2022, 2022.

Darmenova, K., Sokolik, I. N., Shao, Y., Marticorena, B., and Bergametti, G.: Development of a physically based dust emission module within the Weather Research and Forecasting (WRF) model: Assessment of dust emission parameterizations and input parameters for source regions in Central and East Asia, Journal of Geophysical Research: Atmospheres, 114, https://doi.org/10.1029/2008JD011236, 2009.

Deabji, N., Fomba, K. W., El Hajjaji, S., Mellouki, A., Poulain, L., Zeppenfeld, S., and Herrmann, H.: First insights into northern Africa high-altitude background aerosol chemical composition and source influences, Atmospheric Chemistry and Physics, 21, 18 147–18 174, https://doi.org/10.5194/acp-21-18147-2021, 2021.

Di Biagio, C., Formenti, P., Balkanski, Y., Caponi, L., Cazaunau, M., Pangui, E., Journet, E., Nowak, S., Andreae, M. O., Kandler, K., Saeed, T., Piketh, S., Seibert, D., Williams, E., and Doussin, J.-F.: Complex refractive indices and single-scattering albedo of global dust aerosols in the shortwave spectrum and relationship to size and iron content, Atmospheric Chemistry and Physics, 19, 15 503–15 531, https://doi.org/10.5194/acp-19-15503-2019, 2019.

Di Biagio, C., Balkanski, Y., Albani, S., Boucher, O., and Formenti, P.: Direct Radiative Effect by Mineral Dust Aerosols Constrained by New Microphysical and Spectral Optical Data, Geophysical Research Letters, 47, e2019GL086 186, https://doi.org/10.1029/2019GL086186, 2020.

Enete, I.: Harmattan Dust: Composition, Characteristics and Effects on Soil Fertility in Enugu, Nigeria, British Journal of Applied Science & Technology, 2, 72–81, https://doi.org/10.9734/BJAST/2012/950, 2012.

Fomba, K. W., Deabji, N., Barcha, S. E. I., Ouchen, I., Elbaramoussi, E. M., El Moursli, R. C., Harnafi, M., El Hajjaji, S., Mellouki, A., and Herrmann, H.: Application of TXRF in monitoring trace metals in particulate matter and cloud water, Atmospheric Measurement Techniques, 13, 4773–4790, https://doi.org/10.5194/amt-13-4773-2020, 2020.

Fomba, K. W., Quaye, D. T., Achterberg, E. P., Marais, E., and Herrmann, H.: Saharan and Namib Dust Phosphorus Fluxes in the North and South Atlantic Regions, ACS Earth and Space Chemistry, 9, 1465–1478, https://doi.org/10.1021/acsearthspacechem.4c00411, 2025.

Formenti, P., Rajot, J. L., Desboeufs, K., Caquineau, S., Chevaillier, S., Nava, S., Gaudichet, A., Journet, E., Triquet, S., Alfaro, S., Chiari, M., Haywood, J., Coe, H., and Highwood, E.: Regional variability of the composition of mineral dust from western Africa: Results from the AMMA SOP0/DABEX and DODO field campaigns, Journal of Geophysical Research: Atmospheres, 113, https://doi.org/10.1029/2008JD009903, _eprint: https://onlinelibrary.wiley.com/doi/pdf/10.1029/2008JD009903, 2008.

Formenti, P., Schütz, L., Balkanski, Y., Desboeufs, K., Ebert, M., Kandler, K., Petzold, A., Scheuvens, D., Weinbruch, S., and Zhang, D.: Recent progress in understanding physical and chemical properties of African and Asian mineral dust, Atmospheric Chemistry and Physics, 11, 8231–8256, https://doi.org/10.5194/acp-11-8231-2011, 2011.

Formenti, P., Caquineau, S., Desboeufs, K., Klaver, A., Chevaillier, S., Journet, E., and Rajot, J. L.: Mapping the physico-chemical properties of mineral dust in western Africa: mineralogical composition, Atmospheric Chemistry and Physics, 14, 10 663–10 686, https://doi.org/10.5194/acp-14-10663-2014, 2014.

Fuster, B., Sánchez-Zapero, J., Camacho, F., García-Santos, V., Verger, A., Lacaze, R., Weiss, M., Baret, F., and Smets, B.: Quality Assessment of PROBA-V LAI, fAPAR and fCOVER Collection 300 m Products of Copernicus Global Land Service, Remote Sensing, 12, 1017, https://doi.org/10.3390/rs12061017, 2020.

Fécan, F., Marticorena, B., and Bergametti, G.: Parametrization of the increase of the aeolian erosion threshold wind friction velocity due to soil moisture for arid and semi-arid areas, Annales Geophysicae, 17, 149–157, https://doi.org/10.1007/s00585-999-0149-7, 1999.

Gebauer, H., Floutsi, A. A., Hofer, J., Haarig, M., Skupin, A., Engelmann, R., Jimenez, C., Wagner, R., and Baars, H.: Characterization of the annual cycle of atmospheric aerosol over Mindelo, Cabo Verde, by means of continuous multiwavelength lidar observations, Atmospheric Chemistry and Physics, 26, 3439–3465, https://doi.org/10.5194/acp-26-3439-2026, 2026.

Gonçalves Ageitos, M., Obiso, V., Miller, R. L., Jorba, O., Klose, M., Dawson, M., Balkanski, Y., Perlwitz, J., Basart, S., Di Tomaso, E., Escribano, J., Macchia, F., Montané, G., Mahowald, N. M., Green, R. O., Thompson, D. R., and Pérez García-Pando, C.: Modeling dust mineralogical composition: sensitivity to soil mineralogy atlases and their expected climate impacts, Atmospheric Chemistry and Physics, 23, 8623–8657, https://doi.org/10.5194/acp-23-8623-2023, 2023.

Green, R. O., Mahowald, N., Ung, C., Thompson, D. R., Bator, L., Bennet, M., Bernas, M., Blackway, N., Bradley, C., Cha, J., Clark, P., Clark, R., Cloud, D., Diaz, E., Ben Dor, E., Duren, R., Eastwood, M., Ehlmann, B. L., Fuentes, L., Ginoux, P., Gross, J., He, Y., Kalashnikova, O., Kert, W., Keymeulen, D., Klimesh, M., Ku, D., Kwong-Fu, H., Liggett, E., Li, L., Lundeen, S., Makowski, M. D., Mazer, A., Miller, R., Mouroulis, P., Oaida, B., Okin, G. S., Ortega, A., Oyake, A., Nguyen, H., Pace, T., Painter, T. H., Pempejian, J., Garcia-Pando, C. P., Pham, T., Phillips, B., Pollock, R., Purcell, R., Realmuto, V., Schoolcraft, J., Sen, A., Shin, S., Shaw, L., Soriano, M., Swayze, G., Thingvold, E., Vaid, A., and Zan, J.: The Earth Surface Mineral Dust Source Investigation: An Earth Science Imaging Spectroscopy Mission, in: 2020 IEEE Aerospace Conference, pp. 1–15, https://doi.org/10.1109/AERO47225.2020.9172731, 2020.

Gómez Maqueo Anaya, S.: Implementation of mineralogical composition of dust aerosol into COSMO-MUSCAT and application to interpret lidar data, Doctoral dissertation, University of Leipzig, 2025.

Gómez Maqueo Anaya, S., Althausen, D., Faust, M., Baars, H., Heinold, B., Hofer, J., Tegen, I., Ansmann, A., Engelmann, R., Skupin, A., Heese, B., and Schepanski, K.: The implementation of dust mineralogy in COSMO5.05-MUSCAT, Geoscientific Model Development, 17, 1271–1295, https://doi.org/10.5194/gmd-17-1271-2024, 2024.

Gómez Maqueo Anaya, S., Althausen, D., Hofer, J., Haarig, M., Wandinger, U., Heinold, B., Tegen, I., Faust, M., Baars, H., Ansmann, A., Engelmann, R., Skupin, A., Heese, B., and Schepanski, K.: Investigating the link between mineral dust hematite content and intensive optical properties by means of lidar measurements and aerosol modeling, Atmospheric Chemistry and Physics, 25, 9737–9764, https://doi.org/10.5194/acp-25-9737-2025, 2025.

Harrison, A. D., Lever, K., Sanchez-Marroquin, A., Holden, M. A., Whale, T. F., Tarn, M. D., McQuaid, J. B., and Murray, B. J.: The ice-nucleating ability of quartz immersed in water and its atmospheric importance compared to K-feldspar, Atmospheric Chemistry and Physics, 19, 11 343–11 361, https://doi.org/10.5194/acp-19-11343-2019, 2019.

Heinold, B., Helmert, J., Hellmuth, O., Wolke, R., Ansmann, A., Marticorena, B., Laurent, B., and Tegen, I.: Regional modeling of Saharan dust events using LM-MUSCAT: Model description and case studies, Journal of Geophysical Research: Atmospheres, 112, https://doi.org/10.1029/2006JD007443, _eprint: https://agupubs.onlinelibrary.wiley.com/doi/pdf/10.1029/2006JD007443, 2007.

Heinold, B., Tegen, I., Schepanski, K., Tesche, M., Esselborn, M., Freudenthaler, V., Gross, S., Kandler, K., Knippertz, P., Müller, D., Schladitz, A., Toledano, C., Weinzierl, B., Ansmann, A., Althausen, D., Müller, T., Petzold, A., and Wiedensohler, A.: Regional modelling of Saharan dust and biomass-burning smoke: Part 1: Model description and evaluation, Tellus B: Chemical and Physical Meteorology, 63, 781–799, https://doi.org/10.1111/j.1600-0889.2011.00570.x, 2011.

Huneeus, N., Schulz, M., Balkanski, Y., Griesfeller, J., Prospero, J., Kinne, S., Bauer, S., Boucher, O., Chin, M., Dentener, F., Diehl, T., Easter, R., Fillmore, D., Ghan, S., Ginoux, P., Grini, A., Horowitz, L., Koch, D., Krol, M. C., Landing, W., Liu, X., Mahowald, N., Miller, R., Morcrette, J.-J., Myhre, G., Penner, J., Perlwitz, J., Stier, P., Takemura, T., and Zender, C. S.: Global dust model intercomparison in AeroCom phase I, Atmospheric Chemistry and Physics, 11, 7781–7816, https://doi.org/10.5194/acp-11-7781-2011, 2011.

Iversen, J. D. and White, B. R.: Saltation threshold on Earth, Mars and Venus, Sedimentology, 29, 111–119, https://doi.org/10.1111/j.1365-3091.1982.tb01713.x, 1982.

Jahn, L. G., Jahl, L. G., Bland, G. D., Bowers, B. B., Monroe, L. W., and Sullivan, R. C.: Metallic and Crustal Elements in Biomass-Burning Aerosol and Ash: Prevalence, Significance, and Similarity to Soil Particles, ACS Earth and Space Chemistry, 5, 136–148, https://doi.org/10.1021/acsearthspacechem.0c00191, 2021.

Jakobsen, H. A., Berge, E., and Jonson, J. E.: The Multi-layer Eulerian Model: Model Description and Evaluation of Transboundary Fluxes of Sulphur and Nitrogen for One Year, DNMI Research Report 49, Meteorological Synthesizing Centre-West, https://books.google.de/books?id=Lu8ivwEACAAJ, eCE Co-Operative Programme for and Europe, Evaluation of the Long Range Transmission of Air Pollutants in and Meteorological Synthesizing Centre–West (Oslo, Norway), 1997.

Jeong, G. Y. and Achterberg, E. P.: Chemistry and mineralogy of clay minerals in Asian and Saharan dusts and the implications for iron supply to the oceans, Atmospheric Chemistry and Physics, 14, 12 415–12 428, https://doi.org/10.5194/acp-14-12415-2014, 2014.

Journet, E., Desboeufs, K. V., Caquineau, S., and Colin, J.-L.: Mineralogy as a critical factor of dust iron solubility, Geophysical Research Letters, 35, https://doi.org/10.1029/2007GL031589, _eprint: https://agupubs.onlinelibrary.wiley.com/doi/pdf/10.1029/2007GL031589, 2008.

Journet, E., Balkanski, Y., and Harrison, S. P.: A new data set of soil mineralogy for dust-cycle modeling, Atmospheric Chemistry and Physics, 14, 3801–3816, https://doi.org/10.5194/acp-14-3801-2014, 2014.

Kandler, K., Benker, N., Bundke, U., Cuevas, E., Ebert, M., Knippertz, P., Rodríguez, S., Schütz, L., and Weinbruch, S.: Chemical composition and complex refractive index of Saharan Mineral Dust at Izaña, Tenerife (Spain) derived by electron microscopy, Atmospheric Environment, 41, 8058–8074, https://doi.org/10.1016/j.atmosenv.2007.06.047, 2007.

Kandler, K., Schütz, L., Deutscher, C., Ebert, M., Hofmann, H., Jäckel, S., Jaenicke, R., Knippertz, P., Lieke, K., Massling, A., Petzold, A., Schladitz, A., Weinzierl, B., Wiedensohler, A., Zorn, S., and Weinbruch, S.: Size distribution, mass concentration, chemical and mineralogical composition and derived optical parameters of the boundary layer aerosol at Tinfou, Morocco, during SAMUM 2006, Tellus B: Chemical and Physical Meteorology, 61, 32, https://doi.org/10.1111/j.1600-0889.2008.00385.x, 2009.

Kandler, K., Schütz, L., Jäckel, S., Lieke, K., Emmel, C., Müller-Ebert, D., Ebert, M., Scheuvens, D., Schladitz, A., Šegvić, B., Wiedensohler, A., and Weinbruch, S.: Ground-based off-line aerosol measurements at Praia, Cape Verde, during the Saharan Mineral Dust Experiment: microphysical properties and mineralogy, Tellus B, 63, 459–474, https://doi.org/10.1111/j.1600-0889.2011.00546.x, 2011.

Kandler, K., Schneiders, K., Ebert, M., Hartmann, M., Weinbruch, S., Prass, M., and Pöhlker, C.: Composition and mixing state of atmospheric aerosols determined by electron microscopy: method development and application to aged Saharan dust deposition in the Caribbean boundary layer, Atmospheric Chemistry and Physics, 18, 13 429–13 455, https://doi.org/10.5194/acp-18-13429-2018, 2018.

Kelly, J. T., Chuang, C. C., and Wexler, A. S.: Influence of dust composition on cloud droplet formation, Atmospheric Environment, 41, 2904–2916, https://doi.org/10.1016/j.atmosenv.2006.12.008, 2007.

Kezoudi, M., Keleshis, C., Antoniou, P., Biskos, G., Bronz, M., Constantinides, C., Desservettaz, M., Gao, R.-S., Girdwood, J., Harnetiaux, J., Kandler, K., Leonidou, A., Liu, Y., Lelieveld, J., Marenco, F., Mihalopoulos, N., Močnik, G., Neitola, K., Paris, J.-D., Pikridas, M., Sarda-Esteve, R., Stopford, C., Unga, F., Vrekoussis, M., and Sciare, J.: The Unmanned Systems Research Laboratory (USRL): A New Facility for UAV-Based Atmospheric Observations, Atmosphere, 12, 1042, https://doi.org/10.3390/atmos12081042, 2021.

Kezoudi, M., Papetta, A., Kandler, K., Ryder, C. L., Leonidou, A., Keleshis, C., Stopford, C., Thornberry, T., Mamouri, R.-E., Sciare, J., and Marenco, F.: Microphysical and Compositional Differences Between Saharan and Middle Eastern Dust Revealed by UAS Observations, https://doi.org/10.5194/egusphere-2025-5234, 2025.

Kinne, S., Schulz, M., Textor, C., Guibert, S., Balkanski, Y., Bauer, S. E., Berntsen, T., Berglen, T. F., Boucher, O., Chin, M., Collins, W., Dentener, F., Diehl, T., Easter, R., Feichter, J., Fillmore, D., Ghan, S., Ginoux, P., Gong, S., Grini, A., Hendricks, J., Herzog, M., Horowitz,

L., Isaksen, I., Iversen, T., Kirkevåg, A., Kloster, S., Koch, D., Kristjansson, J. E., Krol, M., Lauer, A., Lamarque, J. F., Lesins, G., Liu, X., Lohmann, U., Montanaro, V., Myhre, G., Penner, J., Pitari, G., Reddy, S., Seland, O., Stier, P., Takemura, T., and Tie, X.: An AeroCom initial assessment – optical properties in aerosol component modules of global models, Atmospheric Chemistry and Physics, 6, 1815–1834, https://doi.org/10.5194/acp-6-1815-2006, 2006.

Kok, J. F.: A scaling theory for the size distribution of emitted dust aerosols suggests climate models underestimate the size of the global dust cycle, Proceedings of the National Academy of Sciences, 108, 1016–1021, https://doi.org/10.1073/pnas.1014798108, 2011.

Kok, J. F., Parteli, E. J. R., Michaels, T. I., and Karam, D. B.: The physics of wind-blown sand and dust, Reports on Progress in Physics, 75, 106 901, https://doi.org/10.1088/0034-4885/75/10/106901, 2012.

Kok, J. F., Storelvmo, T., Karydis, V. A., Adebiyi, A. A., Mahowald, N. M., Evan, A. T., He, C., and Leung, D. M.: Mineral dust aerosol impacts on global climate and climate change, Nature Reviews Earth & Environment, 4, 71–86, https://doi.org/10.1038/s43017-022-00379-5, 2023.

Lafon, S., Rajot, J.-L., Alfaro, S. C., and Gaudichet, A.: Quantification of iron oxides in desert aerosol, Atmospheric Environment, 38, 1211–1218, https://doi.org/10.1016/j.atmosenv.2003.11.006, 2004.

Lawrence, C. R. and Neff, J. C.: The contemporary physical and chemical flux of aeolian dust: A synthesis of direct measurements of dust deposition, Chemical Geology, 267, 46–63, https://doi.org/10.1016/j.chemgeo.2009.02.005, 2009.

Li, L., Mahowald, N. M., Miller, R. L., Pérez García-Pando, C., Klose, M., Hamilton, D. S., Gonçalves Ageitos, M., Ginoux, P., Balkanski, Y., Green, R. O., Kalashnikova, O., Kok, J. F., Obiso, V., Paynter, D., and Thompson, D. R.: Quantifying the range of the dust direct radiative effect due to source mineralogy uncertainty, Atmospheric Chemistry and Physics, 21, 3973–4005, https://doi.org/10.5194/acp-21-3973-2021, 2021.

Li, L., Mahowald, N. M., Gonçalves Ageitos, M., Obiso, V., Miller, R. L., Pérez García-Pando, C., Di Biagio, C., Formenti, P., Brodrick, P. G., Clark, R. N., Green, R. O., Kokaly, R., Swayze, G., and Thompson, D. R.: Improved constraints on hematite refractive index for estimating climatic effects of dust aerosols, Communications Earth & Environment, 5, 295, https://doi.org/10.1038/s43247-024-01441-4, 2024.

Lieke, K., Kandler, K., Scheuvens, D., Emmel, C., Von Glahn, C., Petzold, A., Weinzierl, B., Veira, A., Ebert, M., Weinbruch, S., and Schütz, L.: Particle chemical properties in the vertical column based on aircraft observations in the vicinity of Cape Verde Islands, Tellus B: Chemical and Physical Meteorology, 63, 497, https://doi.org/10.1111/j.1600-0889.2011.00553.x, 2011.

Mahowald, N., Albani, S., Kok, J. F., Engelstaeder, S., Scanza, R., Ward, D. S., and Flanner, M. G.: The size distribution of desert dust aerosols and its impact on the Earth system, Aeolian Research, 15, 53–71, https://doi.org/10.1016/j.aeolia.2013.09.002, 2014.

Marinou, E., Paschou, P., Tsikoudi, I., Tsekeri, A., Daskalopoulou, V., Kouklaki, D., Siomos, N., Spanakis-Misirlis, V., Voudouri, K. A., Georgiou, T., Drakaki, E., Kampouri, A., Papachristopoulou, K., Mavropoulou, I., Mallios, S., Proestakis, E., Gkikas, A., Koutsoupi, I., Raptis, I. P., Kazadzis, S., Baars, H., Floutsi, A., Pirloaga, R., Nemuc, A., Marenco, F., Kezoudi, M., Papetta, A., Močnik, G., Díez, J. Y., Ryder, C. L., Ratcliffe, N., Kandler, K., Sudharaj, A., and Amiridis, V.: An Overview of the ASKOS Campaign in Cabo Verde, in: 16th International Conference on Meteorology, Climatology and Atmospheric Physics—COMECAP 2023, p. 200, MDPI, https://doi.org/10.3390/environsciproc2023026200, 2023.

Marticorena, B. and Bergametti, G.: Modeling the atmospheric dust cycle: 1. Design of a soil-derived dust emission scheme, Journal of Geophysical Research: Atmospheres, 100, 16 415–16 430, https://doi.org/10.1029/95JD00690, 1995.

Miffre, A., Cholleton, D., Noël, C., and Rairoux, P.: Investigating the dependence of mineral dust depolarization on complex refractive index and size with a laboratory polarimeter at 180.0° lidar backscattering angle, Atmospheric Measurement Techniques, 16, 403–417, https://doi.org/10.5194/amt-16-403-2023, 2023.

Miltenberger, A. K., Pfahl, S., and Wernli, H.: An online trajectory module (version 1.0) for the nonhydrostatic numerical weather prediction model COSMO, Geoscientific Model Development, 6, 1989–2004, https://doi.org/10.5194/gmd-6-1989-2013, 2013.

Moreno, T., Querol, X., Castillo, S., Alastuey, A., Cuevas, E., Herrmann, L., Mounkaila, M., Elvira, J., and Gibbons, W.: Geochemical variations in aeolian mineral particles from the Sahara–Sahel Dust Corridor, Chemosphere, 65, 261–270, https://doi.org/10.1016/j.chemosphere.2006.02.052, 2006.

Murray, B. J., O'Sullivan, D., Atkinson, J. D., and Webb, M. E.: Ice nucleation by particles immersed in supercooled cloud droplets, Chemical Society Reviews, 41, 6519, https://doi.org/10.1039/c2cs35200a, 2012.

Muñoz Sabater, J. and Copernicus Climate Change Service, S.: ERA5-Land hourly data from 2001 to present, https://doi.org/10.24381/CDS.E2161BAC, type: dataset, 2019.

Møberg, J., Esu, I., and Malgwi, W.: Characteristics and constituent composition of Harmattan dust falling in Northern Nigeria, Geoderma, 48, 73–81, https://doi.org/10.1016/0016-7061(91)90007-G, 1991.

Nickovic, S., Vukovic, A., Vujadinovic, M., Djurdjevic, V., and Pejanovic, G.: Technical Note: High-resolution mineralogical database of dust-productive soils for atmospheric dust modeling, Atmospheric Chemistry and Physics, 12, 845–855, https://doi.org/10.5194/acp-12-845-2012, 2012.

Obiso, V., Gonçalves Ageitos, M., Pérez García-Pando, C., Perlwitz, J. P., Schuster, G. L., Bauer, S. E., Di Biagio, C., Formenti, P., Tsigaridis, K., and Miller, R. L.: Observationally constrained regional variations of shortwave absorption by iron oxides emphasize the cooling effect of dust, Atmospheric Chemistry and Physics, 24, 5337–5367, https://doi.org/10.5194/acp-24-5337-2024, 2024.

Panta, A., Kandler, K., Alastuey, A., González-Flórez, C., González-Romero, A., Klose, M., Querol, X., Reche, C., Yus-Díez, J., and Pérez García-Pando, C.: Insights into the single-particle composition, size, mixing state, and aspect ratio of freshly emitted mineral dust from field measurements in the Moroccan Sahara using electron microscopy, Atmospheric Chemistry and Physics, 23, 3861–3885, https://doi.org/10.5194/acp-23-3861-2023, 2023.

Paris, R., Desboeufs, K. V., Formenti, P., Nava, S., and Chou, C.: Chemical characterisation of iron in dust and biomass burning aerosols during AMMA-SOP0/DABEX: implication for iron solubility, Atmospheric Chemistry and Physics, 10, 4273–4282, https://doi.org/10.5194/acp-10-4273-2010, 2010.

Perlwitz, J. P., Pérez García-Pando, C., and Miller, R. L.: Predicting the mineral composition of dust aerosols – Part 1: Representing key processes, Atmospheric Chemistry and Physics, 15, 11 593–11 627, https://doi.org/10.5194/acp-15-11593-2015, 2015a.

Perlwitz, J. P., Pérez García-Pando, C., and Miller, R. L.: Predicting the mineral composition of dust aerosols – Part 2: Model evaluation and identification of key processes with observations, Atmospheric Chemistry and Physics, 15, 11 629–11 652, https://doi.org/10.5194/acp-15-11629-2015, 2015b.

Poggio, L., de Sousa, L. M., Batjes, N. H., Heuvelink, G. B. M., Kempen, B., Ribeiro, E., and Rossiter, D.: SoilGrids 2.0: producing soil information for the globe with quantified spatial uncertainty, SOIL, 7, 217–240, https://doi.org/10.5194/soil-7-217-2021, 2021.

Prigent, C., Aires, F., Rossow, W. B., and Robock, A.: Sensitivity of satellite microwave and infrared observations to soil moisture at a global scale: Relationship of satellite observations to in situ soil moisture measurements, Journal of Geophysical Research: Atmospheres, 110, https://doi.org/10.1029/2004JD005087, 2005.

Pérez García-Pando, C., Miller, R. L., Perlwitz, J. P., Rodríguez, S., and Prospero, J. M.: Predicting the mineral composition of dust aerosols: Insights from elemental composition measured at the Izaña Observatory, Geophysical Research Letters, 43, https://doi.org/10.1002/2016GL069873, 2016.

Rieder, M., Cavazzini, G., D'yakonov, Y. S., Frank-Kamenetskii, V. A., Gottardi, G., Guggenheim, S., Koval', P. W., Müller, G., Neiva, A. M. R., Radoslovich, E. W., Robert, J.-L., Sassi, F. P., Takeda, H., Weiss, Z., and Wones, D. R.: Nomenclature of the Micas, Clays and Clay Minerals, 46, 586–595, https://doi.org/10.1346/CCMN.1998.0460513, 1998.

Scanza, R. A., Mahowald, N., Ghan, S., Zender, C. S., Kok, J. F., Liu, X., Zhang, Y., and Albani, S.: Modeling dust as component minerals in the Community Atmosphere Model: development of framework and impact on radiative forcing, Atmospheric Chemistry and Physics, 15, 537–561, https://doi.org/10.5194/acp-15-537-2015, 2015.

Schepanski, K., Tegen, I., Laurent, B., Heinold, B., and Macke, A.: A new Saharan dust source activation frequency map derived from MSG-SEVIRI IR-channels, Geophysical Research Letters, 34, https://doi.org/10.1029/2007GL030168, 2007.

Schepanski, K., Tegen, I., and Macke, A.: Saharan dust transport and deposition towards the tropical northern Atlantic, Atmospheric Chemistry and Physics, 9, 1173–1189, https://doi.org/10.5194/acp-9-1173-2009, 2009.

Schepanski, K., Mallet, M., Heinold, B., and Ulrich, M.: North African dust transport toward the western Mediterranean basin: atmospheric controls on dust source activation and transport pathways during June–July 2013, Atmospheric Chemistry and Physics, 16, 14 147–14 168, https://doi.org/10.5194/acp-16-14147-2016, 2016.

Schepanski, K., Heinold, B., and Tegen, I.: Harmattan, Saharan heat low, and West African monsoon circulation: modulations on the Saharan dust outflow towards the North Atlantic, Atmospheric Chemistry and Physics, 17, 10 223–10 243, https://doi.org/10.5194/acp-17-10223-2017, 2017.

Scheuvens, D., Schütz, L., Kandler, K., Ebert, M., and Weinbruch, S.: Bulk composition of northern African dust and its source sediments — A compilation, Earth-Science Reviews, 116, 170–194, https://doi.org/10.1016/j.earscirev.2012.08.005, 2013.

Seinfeld, J. H. and Pandis, S. N.: Atmospheric Chemistry and Physics: From Air Pollution to Climate Change, 3rd Edition \textbar Wiley, John Wiley & Sons, Hoboken, 3 edn., https://www.wiley.com/en-us/Atmospheric+Chemistry+and+Physics%3A+From+Air+Pollution+to+Climate+Change%2C+3rd+Edition-p-9781118947401, 2016.

Shao, Y., Wyrwoll, K.-H., Chappell, A., Huang, J., Lin, Z., McTainsh, G. H., Mikami, M., Tanaka, T. Y., Wang, X., and Yoon, S.: Dust cycle: An emerging core theme in Earth system science, Aeolian Research, 2, 181–204, https://doi.org/10.1016/j.aeolia.2011.02.001, 2011.

Sokolik, I. N. and Toon, O. B.: Incorporation of mineralogical composition into models of the radiative properties of mineral aerosol from UV to IR wavelengths, Journal of Geophysical Research: Atmospheres, 104, 9423–9444, https://doi.org/10.1029/1998JD200048, 1999.

Song, Q., Ginoux, P., Gonçalves Ageitos, M., Miller, R. L., Obiso, V., and Pérez García-Pando, C.: Modeling impacts of dust mineralogy on fast climate response, Atmospheric Chemistry and Physics, 24, 7421–7446, https://doi.org/10.5194/acp-24-7421-2024, 2024.

Souza, E. J. D. S., Fomba, K. W., Anaya, S. G. M., Schepanski, K., Freire, S. M., Materić, D., Reemtsma, T., and Herrmann, H.: Particle-bound mercury in Saharan dust-loaded particulate matter in Cabo Verde, Journal of Hazardous Materials, 487, 137 053, https://doi.org/10.1016/j.jhazmat.2024.137053, 2025.

Stein, A. F., Draxler, R. R., Rolph, G. D., Stunder, B. J. B., Cohen, M. D., and Ngan, F.: NOAA's HYSPLIT Atmospheric Transport and Dispersion Modeling System, Bulletin of the American Meteorological Society, 96, 2059–2077, https://doi.org/10.1175/BAMS-D-14-00110.1, 2015.

Stocker, T. F., Qin, D., Plattner, G.-K., Tignor, M., Allen, S. K., Boschung, J., Nauels, A., Xia, Y., Bex, V., and Midgley, P. M.: Climate Change 2013: The Physical Science Basis, Tech. rep., Intergovernmental Panel on Climate Change, Working Group I Contribution to the IPCC Fifth Assessment Report (AR5)(Cambridge University Press, Cambridge, United Kingdom and New York, NY, USA.), 1535 pp., 2013.

Tegen, I., Harrison, S. P., Kohfeld, K., Prentice, I. C., Coe, M., and Heimann, M.: Impact of vegetation and preferential source areas on global dust aerosol: Results from a model study, Journal of Geophysical Research: Atmospheres, 107, AAC 14–1–AAC 14–27, https://doi.org/10.1029/2001JD000963, 2002.

Tegen, I., Schepanski, K., and Heinold, B.: Comparing two years of Saharan dust source activation obtained by regional modelling and satellite observations, Atmospheric Chemistry and Physics, 13, 2381–2390, https://doi.org/10.5194/acp-13-2381-2013, 2013.

Tesche, M., Gross, S., Ansmann, A., Müller, D., Althausen, D., Freudenthaler, V., and Esselborn, M.: Profiling of Saharan dust and biomass-burning smoke with multiwavelength polarization Raman lidar at Cape Verde, Tellus B: Chemical and Physical Meteorology, 63, 649–676, https://doi.org/10.1111/j.1600-0889.2011.00548.x, 2011.

Wolke, R. and Knoth, O.: Implicit–explicit Runge–Kutta methods applied to atmospheric chemistry-transport modelling, Environmental Modelling & Software, 15, 711–719, https://doi.org/10.1016/S1364-8152(00)00034-7, 2000.

Wolke, R., Schröder, W., Schrödner, R., and Renner, E.: Influence of grid resolution and meteorological forcing on simulated European air quality: A sensitivity study with the modeling system COSMO–MUSCAT, Atmospheric Environment, 53, 110–130, https://doi.org/10.1016/j.atmosenv.2012.02.085, 2012.

Zhang, L., Gong, S., Padro, J., and Barrie, L.: A size-segregated particle dry deposition scheme for an atmospheric aerosol module, Atmospheric Environment, 35, 549–560, https://doi.org/10.1016/S1352-2310(00)00326-5, 2001.

Zhang, X. L., Wu, G. J., Zhang, C. L., Xu, T. L., and Zhou, Q. Q.: What is the real role of iron oxides in the optical properties of dust aerosols?, Atmospheric Chemistry and Physics, 15, 12 159–12 177, https://doi.org/10.5194/acp-15-12159-2015, 2015.

Zhang, Y., Saito, M., Yang, P., Schuster, G., and Trepte, C.: Sensitivities of Spectral Optical Properties of Dust Aerosols to Their Mineralogical and Microphysical Properties, Journal of Geophysical Research: Atmospheres, 129, e2023JD040 181, https://doi.org/10.1029/2023JD040181, 2024.